A combined experimental and modelling investigation of an overground compressed-air energy storage system with a reversible liquid-piston gas compressor/expander

7 authors, including:

Mansoureh Khaljani
Queen's University Belfast
2 PUBLICATIONS   **7** CITATIONS

Paul Sapin
Imperial College London
53 PUBLICATIONS   **393** CITATIONS

Christos N. Markides
Imperial College London
451 PUBLICATIONS   **9,015** CITATIONS

Yasser Mahmoudi Larimi
The University of Manchester
84 PUBLICATIONS   **1,652** CITATIONS

Some of the authors of this publication are also working on these related projects:

Combustion Noise View project

Modelling Distributed Energy Resources View project

A Combined Experimental and Modelling Investigation of an Overground Compressed-Air Energy Storage System with a Reversible Liquid-Piston Gas Compressor/Expander

M. Khaljani [a,b], J. Harrison [b], D. Surplus [c], A. Murphy [a], P. Sapin [d], C. N. Markides [d,*], Y. Mahmoudi [a,e,*]

[a] *School of Mechanical and Aerospace Engineering, Queen's University Belfast, Belfast, BT9 5AG, UK*

[b] *South West College, Cookstown, BT80 8DN, UK*

[c] *B9 Energy Group, Millbrook Industrial Estate, Larne, BT40 2SF, UK*

[d] *Clean Energy Processes (CEP) Laboratory, Department of Chemical Engineering, Imperial College London, South Kensington Campus, London SW7 2AZ, UK*

[e] *Department of Mechanical, Aerospace and Civil Engineering, The University of Manchester, M13 9PL, UK*

Corresponding authors: Emails: yasser.mahmoudilarimi@manchester.ac.uk; c.markides@imperial.ac.uk

Abstract

In the present work, we consider a small-scale overground compressed-air energy storage (CAES) system intended for use in micro-grid power networks. This work goes beyond previous efforts in the literature by developing and showing results from a first-of-a-kind small-scale (20 kWh) near-isothermal CAES system employing a novel, reversible liquid-piston gas compressor and expander (LPGC/E). Additionally, we extend our study to assessments, for the first time, of the economic and environmental characteristics of these small-scale overground CAES systems through a combination of experimental, thermodynamic, technoeconomic and environmental analyses. Five system configurations are considered: (1) $CAES_{base}$, which is the base-case system; (2) $CAES_{plate}$, in which parallel plates are inserted into the LPGC/E as a heat exchanger for achieving near-isothermal compression and expansion; (3) $CAES_{PCM}$, in which a phase change material (PCM) is employed to store thermal energy from the compressed air during charging that is later recovered during discharge; (4) $CAES_{PCM\&plate}$, which is a combination of the $CAES_{plate}$ and $CAES_{PCM}$ arrangements; and (5) $CAES_{heater}$, in which a heater is utilised instead of the PCM to preheat the compressed air during discharge. A prototype was developed for the $CAES_{base}$ system in order to collect data for validation of a computational design tool. Results show that the $CAES_{PCM\&plate}$ system exhibits the highest roundtrip efficiency of 63%, as well as the shortest payback period of 7 years; the latter with the inclusion of governmental incentives and an electricity smart export guarantee (SEG) support rate of 5.5 p/kWh (6.8 ¢/kWh). The $CAES_{PCM\&plate}$ system configuration is found to be cost-effective even without incentives, with a payback period of 10 years. This system is also associated with 71 tonnes of fuel consumption savings and reduced CO_2 emissions amounting to 51 tonnes over a lifetime of 20 years.

1

Nomenclature

Variables			t	Time (s, h)
A	Surface area (m^2)		u	Internal energy (J)
ATC	Annual total cost ($)		U	Overall heat transfer coefficient (W/m^2 K)
ATI	Annual total income ($)		V	Volume (m^3)
ATP	Annual total profit ($)		v	Velocity (m/s)
c	Price ($/Wh, $/L)		W	Work (J, Wh)
c_p	Specific heat capacity (J/kg K)		$\dot{W}$	Power (W)
CEE	Charging electricity efficiency (-)		*Abbreviations*	
CI	Cost index (-)		LPGC	Liquid piston gas compressor
DPP	Dynamic payback period (year)		LMTD	Log mean temperature difference
D	Diameter (m)		O&M	Operation and maintenance
D_h	Hydraulic diameter (m)		PCM	Phase change material
d_i	Inner diameter (m)		TES	Thermal energy storage
d_o	Outer diameter (m)		*Greek symbols*	
E_s	Energy storage (J)		η	Efficiency (-)
f_m	Material factor		α	Heat transfer coefficient (W/m^2 K)
f_d	Design factor		Δ	Difference (-)
f_p	Pressure factor		ρ	Density (kg/m^3)
h	Specific enthalpy (J/kg)		μ	Viscosity (kg/m s)
H	Enthalpy (J)		δ	Thickness (m)
i	Displacement position counter (-)		γ	Specific heat ratio (-)
j	Number of ducts counter (-)		*Subscripts and superscripts*	
k	Conductivity (W/m K)		air	Air
l	Length (m)		ax	Axial
L	Height of water/air (m)		AST	Air-storage tank
L_z	Distance between the parallel plates (m)		base	Base
m	Mass (kg)		chg	Charge
M	Number of ducts (-)		comp	Compressor, Compression
$\dot{m}$	Mass flow rate (kg/s)		dchg	Discharge
n	Total discretisation number (-)		exp	Expander, Expansion
N	Discretisation number (-)		f	Fluid
NPV	Net present value ($)		gen	Generator
Nu	Nusselt number (-)		HX	Heat exchanger
P	Pressure (Pa, bar)		htr	Heater
PD	Power density (W/m^3)		in	Input
PEC	Purchase cost of component ($)		ins	Insert
Pr	Prandtl number (-)		int	Interface
Q	Heat/thermal energy (J), Flow rate (L/min)		out	Output
$\dot{Q}$	Heat transfer rate (W)		p	Plate
Re	Reynolds number (-)		pump	Pump
R	Thermal resistance (m^2/W)		ref	Reference
R_g	Gas constant (J/mol.K)		s	Storage
r_d	Discount rate (-)		tot	Total
r_i	Inflation rate (-)		w	Wall
r_p	Pressure ratio (-)		wat	Water
T	Temperature (K)		WT	Water tank
TIC	Total investment cost ($)		y	Year

1.   Introduction

Although increasing the share of energy produced from renewable sources offers the benefits of lowering fossil-fuel use and emissions, the high intermittency of most environmentally favourable sources (e.g., wind, solar) remains a great challenge, and matching energy supply to demand requires dispatchable and flexible energy provision. A more extensive utilisation of renewable sources in the energy mix thus relies on the deployment of efficient energy storage technologies across scales, both in time and space, in order to store excess energy generated during periods of low demand and to use this during periods of high demand [1].

Several candidate technologies have been proposed for grid-scale (i.e., large-scale) electricity storage [2], including pumped hydro energy storage (PHES), electrochemical/flow batteries, pumped-thermal electricity storage (PTES) [3-7], liquid-air energy storage (LAES) [8-11], and compressed-air energy storage (CAES). PHES technology is the most mature and widely used but its installation is limited by natural, geological constraints [12, 13]. NaS batteries are one type of electrochemical battery solution suitable for large-scale distribution grid support, renewables integration and high-value grid services [14], however, this technology has relatively high capital costs (1000-3000 $/kW), high operational temperature requirements, short lifetimes (10-15 years), as well as safety challenges relative to mechanical (e.g., PHES) or thermo-mechanical systems (e.g., PTES, LAES, or CAES).

CAES is second to PHES in terms of commercial bulk energy storage available today. CAES is generally acknowledged to be an economically competitive means of providing large-scale energy storage with an expected lifetime between 20-60 years and a capital cost in the range 400-800 $/kW [1]. Its power rating (5-300 MW) is significantly higher than those associated with battery technologies [1]. Two conventional (so-called diabatic) CAES plants are currently in commercial operation. The Huntorf power station in Germany (290 MWe) began operation in 1978, has a total efficiency close to 42% and uses natural gas to assist combustion in the energy release process [15]. The McIntosh plant in the USA (110 MWe) exhibits an improved roundtrip efficiency of 54%, achieved by means of waste-heat recovery and the utilisation of equipment for recycling the exhaust heat of the combustion system [16]. In these CAES systems, the air pressure is increased up to 80 bar through a power-driven, multi-stage, inter-cooled compression process, thus releasing part of the generated heat to the atmosphere, while the remaining extra thermal energy is dissipated during the storage of the high-pressure air. Energy is recovered when required through the multi-stage expansion of the high-pressure air at near-ambient temperature, which requires additional heat to be provided.

In both diabatic-CAES plants mentioned, this extra heat is supplied by the combustion of natural gas in inter-stage combustion chambers.

Conventional CAES plants thus present two main drawbacks: (i) heat losses during the compression process lower the roundtrip efficiency (although some heat generated during the compression process can be recuperated to heat up the air prior to expansion in certain operating conditions); and (ii) their dependency on fossil-fuel sources for heating lead to unwanted emissions [17]. To avoid using fossil fuels and improve the roundtrip efficiency, adiabatic compressed-air energy storage (A-CAES) was proposed [18]. In an A-CAES storage system, the thermal energy of the compressed air is stored in a thermal energy storage (TES) system. During the discharge process, the stored high-pressure and cold air is pre-heated using the stored heat energy in the TES before expansion. Although A-CAES systems offer a theoretical roundtrip efficiency of up to 70%, pilot-scale systems have exhibited lower efficiencies [19]. Wang et al. [20], for example, reported an experimentally measured roundtrip efficiency value of 23% for their CAES system. Also of note here is a pilot-scale CAES demonstrator developed in an unused tunnel in Switzerland [19], which was reported as having an efficiency of 63-74%, although this system was not a complete cycle and did not feature a turbine, with the air after the compressors being heated using electric heaters before being storing in TES units [19].

To overcome the drawback of conventional air compressors, the near-isothermal reversible liquid-piston gas compressor/expander (LPGC/E) principle was introduced [21]. LPGC/Es utilise a rising column of liquid (e.g., water) in a fixed-volume cylinder to compress a gas (e.g., air or hydrogen). The water enters the cylinder at high pressure driven by a hydraulic pump [22]. As the water fills the cylinder, the volume of air at the top of the cylinder is compressed up to a desired pressure. The main advantage of the liquid piston is that it offers the possibility of inserting heat absorbing media (metal plates or foams) into the LPGC/E cylinder in order to enhance heat transfer from the compressed air [23]. This enables near-isothermal compression and expansion processes, thereby improving overall efficiency of CAES systems [23]. Another, important advantage of the LPGC/E is that it eliminates the mechanical sliding seals associated with kinematic compressors, and moreover, the liquid-piston compressor can be reversed and used as expander in order to produce power. The sealing of a liquid piston gives an advantage over traditional solid-piston devices in terms of power consumption, as it removes thermodynamic losses due to mass leakage [22], however, unsteady heat losses are also of interest in this component and should be minimised [24, 25].

Van de Ven and Li [21] simulated and compared the performance of a LPGC/E and a

reciprocating, solid-piston compressor under similar operating conditions. Their results indicate that the liquid piston decreases the energy consumption by 19% over the reciprocating piston. Other studies [26-29] were conducted to improve the performance of LPGC/Es. In this regard, Zhang et al. [29] deployed interrupted plate heat exchangers with different materials in an LPGC/E aiming to achieve a near-isothermal compression process by increasing the heat transfer rate from the gas during compression. The authors found that the temperature distribution over the interrupted plate heat exchanger depends on the plate material and thickness. Zhang et al. [27] developed a design for minimising the temperature rise in the compressor during compression by using two types of porous media. They considered open-cell metal foams and interrupted plates. Their simulation results show that the metal-foam inserts can lower the air temperature rise, from 575 K to 215 K [27].

Recently, Patila et al. [30] tested experimentally metal wire meshes as heat transfer inserts in a liquid-piston compressor for the compression of air from atmospheric pressure to about 280 kPa pressure (pressure ratio of 2.8). They considered different wire diameters and meshes made from both aluminium and copper under various compression stroke times. Their results demonstrated a shift in the compression process towards near-isothermal conditions, with improved isothermal efficiency, from 82-84% to 88-90%. In another work, Patil and Rob [31] introduced a heat-transfer enhancement technique using aqueous foam in a liquid-piston compressor to achieve near-isothermal compression. Experiments were undertaken for air compression at low pressure (1 to 3 bar). These results showed that the use of aqueous foams in the compression chamber could be highly effective in reducing the air temperature during the compression process. They further showed that using a compression chamber fully filled with aqueous foam leads to a 4-8% improvement in efficiency for a compression ratio of 2.5.

Compared to large-scale CAES systems that rely almost invariably on underground air storage in caverns, small-scale overground CAES systems with their highly flexible and adaptable characteristics have attracted interest in recent years [32]. Overground CAES systems do not have the limitations imposed by specific underground geological features and can be used for urban peak shaving [32, 33]. Batteries are the most mature energy storage technology for small-scale deployment, and a significant amount of research has been dedicated to reducing costs and improving lifetime and cycle life of batteries for deployment at larger scales, particularly lithium ion batteries which have a high roundtrip efficiency, energy density and peak power capabilities [33]. Although the cost of lithium-ion batteries is falling rapidly, much progress remains to be made in the areas of lifetime and safety [33]. Hence, overground CAES systems are also being developed as alternatives to in for micro-grid scale applications [32, 33].

Previous research on CAES systems has demonstrated the feasibility of small-scale CAES [32, 33]. However, the existing pilot projects exhibit high specific costs, low roundtrip efficiencies, either due to the low performance of the compressor or expansion machines (e.g., see Ref. [20]), or in the need to utilise additional electric heaters prior to expansion in order to overcome the significant heat losses during the compression process [19]. Although reversible liquid-piston gas compressors/expanders (LPGC/Es) show great efficiency improvement potential, no field-scale near-isothermal CAES system has been developed. Furthermore, the economic and environmental aspects of CAES with LPGC/E have not been examined. There is thus a lack of reliable data to explore the full technoeconomic potential of this potentially disruptive energy-storage solution. This highlights the need for comprehensive modelling and design tools to develop the technology and the need to demonstrate experimentally the performance of a high-efficiency, high-energy-density CAES system with a LPGC/E.

Therefore, the present work aims to fill these gaps by investigating, via a combination of complementary experimental and modelling methods, a novel overground CAES system with a reversible liquid-piston compressor/expander capable of near-isothermal compression and expansion. A comprehensive set of experimental, thermodynamic and technoeconomic analyses of such a system is conducted. Data are collected from a custom experimental testing facility to verify the accuracy of a reduced-order model. The validated model is then used to predict the system's efficiency, total investment cost, total annual profit and payback period as well as CO_2 emissions and potential fossil fuel savings over a typical system lifetime.

2.   Description of proposed system

Figure 1(a) illustrates the CAES base-case system, which compresses air from 1 bar (0.1 MPa) to 200 bar (20 MPa). The system contains a LPGC/E, air compressor, regulator, air-storage tanks, water tank, reversible hydraulic pump and valves. The storage process occurs in two steps to reduce the size of the water pump and hence reduce the total cost of the system. In the first step, the air is compressed from 1 to 9 bar by the air compressor (from State 1 to 2, Figure 1(a)). The hot compressed air is then stored in the 9-bar air-storage tank, where it cools down to near-ambient temperature. With the Valve 1 open, the 9-bar air (State 3) passes through a regulator, where its pressure is regulated at 8 bar (State 4). The 8-bar compressed air then flows into the LPGC/E (State 5). In order to compress the air from 8 to 200 bar, the water pressurised by the reversible pump (State 8 to 9) is fed into the LPGC/E. As the water level rises in the cylinder, the air above the

water is compressed up to 200 bar. At the end of the compression process, the compressed air flows through Valve 2 (from State 6 to State 7) and is stored in the high-pressure air-storage tank.

To use the stored energy during the discharge phase, the compressed air enters the LPGC/E at State 13 where it expands from 200 bar down to 2 bar. Air expansion to a pressure above ambient helps a fast discharge of air and water from the LPGC/E to be ready for the next charging phase. As the air expands in the LPGC/E, work is extracted as the water is withdrawn through Valve 3 from States 15 and 16 and then through the reversible pump (States 16 to 17). It is well documented within the pump industry that running a centrifugal pump in reverse will create a turbine effect, so-called pump as turbine (PAT). The function of a PAT is comparable to that of any turbine to convert kinetic and pressure energy of the fluid into mechanical energy of the runner [34]. Unlike turbines and expanders, which need to be manufactured according to the system specifications, pumps are a very common piece of equipment widely available in different sizes. When operating in reserve and used as a turbine, the rotor moves in the opposite direction, or in reverse, as to when it is operating as a pump. In this manner, it allows the motor to generate electrical power.

In this work, in addition to the base-case system (CAES$_{base}$), four other system configurations are analysed in terms of system performance and CO_2-emission reduction, while minimising the system cost. These configurations are described as follows:
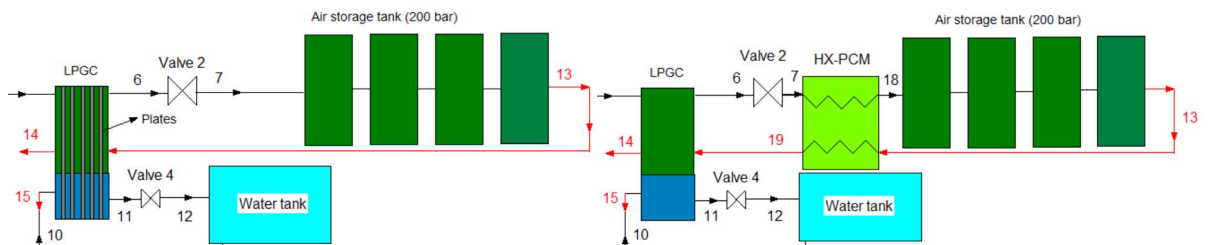
1. In the CAES$_{plate}$ configuration shown in Figure 1(b), five parallel plates are used as a heat exchanger in the LPGC/E cylinder to achieve near-isothermal compression or expansion. This is used to increase the efficiency of the compression/expansion processes in the LPGC/E. During the compression process, the heat is absorbed from the hot air by the inserts, so as to achieve near-isothermal compression. In addition, a near-isothermal expansion is achieved thanks to the heat released by the plate inserts.

2. The CAES$_{PCM}$ configuration, shown in Figure 1(c), differs from the CAES$_{base}$ configuration in that a heat exchanger with a phase-change material (PCM) is used to store the thermal energy of the hot air before storing the compressed air in the storage tank. The stored thermal energy is then used to heat up the compressed air through the expansion phase. This configuration does not improve the compression efficiency of the LPGC/E, but is aimed at improving the LPGC/E power output.

3. The CAES$_{PCM\&plate}$ system is a combination of the CAES$_{PCM}$ and CAES$_{plate}$ configurations, as shown in Figure 1(d), where the parallel plate inserts are used to improve the compression efficiency and the PCM is used to improve the expansion efficiency. The parallel plates decrease the input compression work in the compression

process and preheating the compressed air by the PCM heat exchanger improves the power output by the LPGC/E in the expansion process.
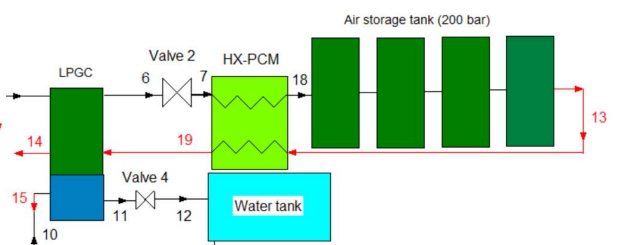
4. The CAES$_{heater}$ configuration, shown in Figure 1(e), is similar to the base-case configuration CAES$_{base}$, though with an additional heater used to preheat the compressed air before expansion in the LPGC/E. It is assumed that natural gas is burned to increase the air temperature to the same value as that in the CAES$_{PCM}$ configuration before expansion.
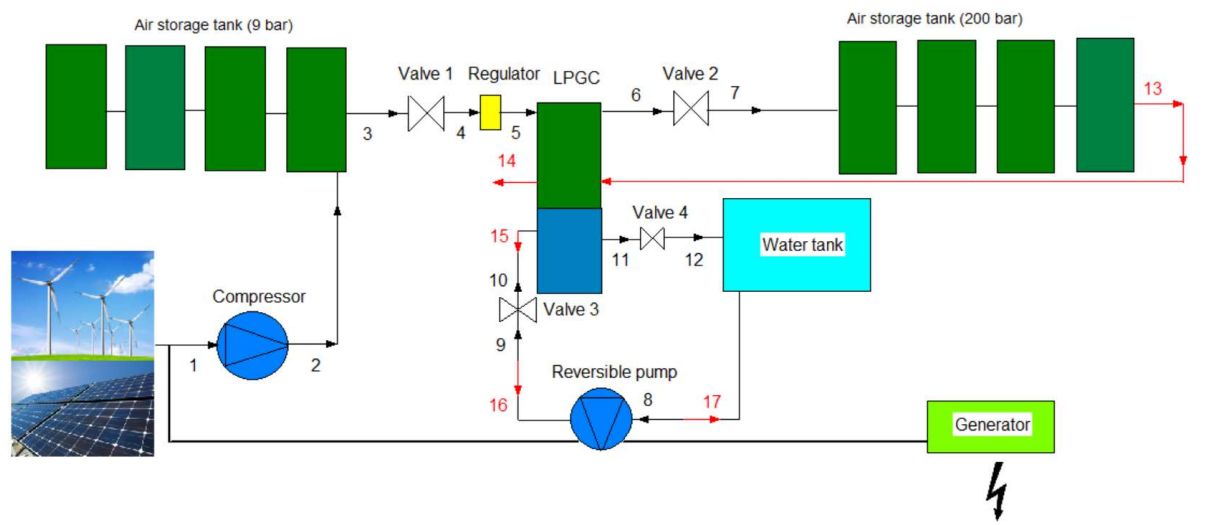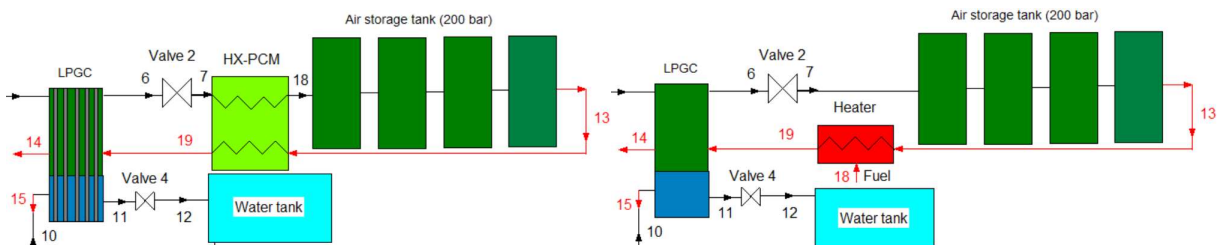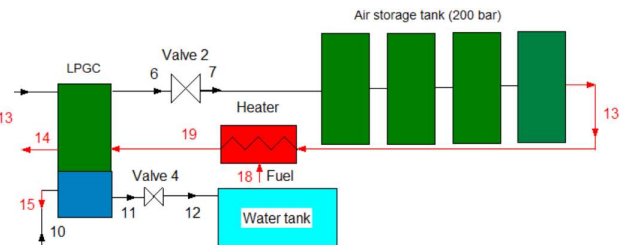

(a)

(b)   (c)

(d)   (e)

Figure 1. Schematic diagrams of CAES systems with LPGC/E showing: (a) CAES$_{base}$ base-case configuration; (b) near-isothermal LPGC/E operation with parallel plates inside the LPGC/E (CAES$_{plate}$); (c) storage of thermal energy in a PCM heat exchanger during air

compression, and reuse for preheating the air before expansion (CAES$_{PCM}$); (d) placement of parallel plates inside the LPGC/E for near-isothermal compression plus use of a PCM heat exchanger for thermal energy storage during air compression and reuse for preheating the air before expansion (CAES$_{PCM\&plate}$); and (e) system configuration wherein a heater is used to preheat the air before expansion by burning a fuel (CAES$_{heater}$).

It is worth noting that, compared to conventional CAES systems that require a compressor and a separate expander, the CAES system proposed here employs a single, reversible LPGC/E component that operates both as a compressor and expander using a reversible pump (see Figure 1). In conventional systems, multiple compressor and/or expander stages with intercoolers are required to limit the temperature rise/drop during the compression/expansion processes. Furthermore, additional heat exchangers are required in these conventional systems to extract excess (and release stored) thermal energy from the compressed air (and to the air prior expansion). This allows the presently proposed system to be less complex overall, fewer components and loss mechanisms, even though heat transfer surfaces can be placed within the LPGC/E of the proposed system to promote near-isothermal compression and expansion.

3.   Experimental apparatus

In order to promote our understanding of the operation and performance characteristics of the proposed CAES technology, and to validate a model of this system (see Section 4), a lab-scale testing facility (Figure 2) of the base-case configuration, CAES$_{base}$, has been developed at Queen's University of Belfast. Time-dependent, temperature and pressure measurements were performed at different locations to monitor the CAES system's time-varying behaviour during operation, and to determine its performance, including roundtrip efficiency.

Ambient air is compressed through a low-pressure compressor, and a 150-L vertical air-storage tank rated at 9 bar is used in this work. Prior to start-up, the 9-bar air-storage tank is filled with compressed air, which it cools to ambient temperature. During operation of the system, the 9-bar air-storage tank is constantly filled with the compressed air, where the mass flow rate of the inlet air is the same as that leaving the storage tank. During the compression phase, a valve is opened, and the air enters the LPGC/E cylinder at 8 bar. Then, the main pump supplies the high-pressure water to the LPGC/E cylinder to compress the air up to 40 bar. At the end of the compression phase, a valve is opened at the top of the cylinder and the compressed

air is stored in a 40-bar air-storage tank. Finally, the valve is opened, and the water is withdrawn from the LPGC/E cylinder into the water tank. In this prototype, two LPGC/Es work in parallel allowing the system to work continuously to avoid shutting the hydraulic pump on and off. The experimental apparatus in its present form does not feature an expansion device; this is part of the ongoing research by the authors. Nevertheless, this component was included in the modelling description of the overall CAES system in this work.

The system is controlled by a programmable logic controller (PLC) and time-resolved data are recorded by a data-acquisition (DAQ) device. The time-varying volume of air in the cylinder is deduced from the water inlet flow rate, measured with a SM7000 magnetic-inductive flow meter. Air pressure is measured directly with a pressure transmitter (Model A-10; www.wika.co.uk). The bulk, mass-averaged air temperature is obtained from the air volume and pressure measurements using the ideal gas law [23]. The initial temperature of the air in the tank (before air charging), and the air temperature downstream of the 9-bar air storage tank are measured using a platinum resistance thermometer (PRT) (Model Pt100; https://uk.rs-online.com). Additionally, a PRT is located at the top cap of the cylinder to measure the final air temperature after compression. However, due to the relatively slow response time of the PRTs and the presence of large thermal gradients during compression, these temperature measurements are considered trustworthy only under steady-state conditions [23]. Therefore, the time-varying temperature of the air is calculated from pressure and density using a lookup table based on ideal gas properties [23].

The LPGC/E cylinder is made of stainless steel and has a height of 1.1 m, an internal diameter of 0.08 m and a wall thickness of 0.01 m. The empty volume of the cylinder is 0.00553 m^3. A boosted axial piston water pump (Janus axial piston pump; www.waterhydraulics.co.uk) at 70 cc/rev circulates water through the circuit. A DN12 relief valve is used to divert a portion of this flow back to the tank. The LPGC/E cylinder can be safely pressurised up to 200 bar. However, due to the cost and size limitation of the reversible pump, the experimental data is collected when the system is charged to 40 bar. The experimental data are collected only for the compression (charging) process and are used to validate the modelling tools developed and presented in detail in the next section. The model is then used to study the LPGC/E CAES system for both charging and discharging processes working in envisaged operating conditions, at 200 bar.
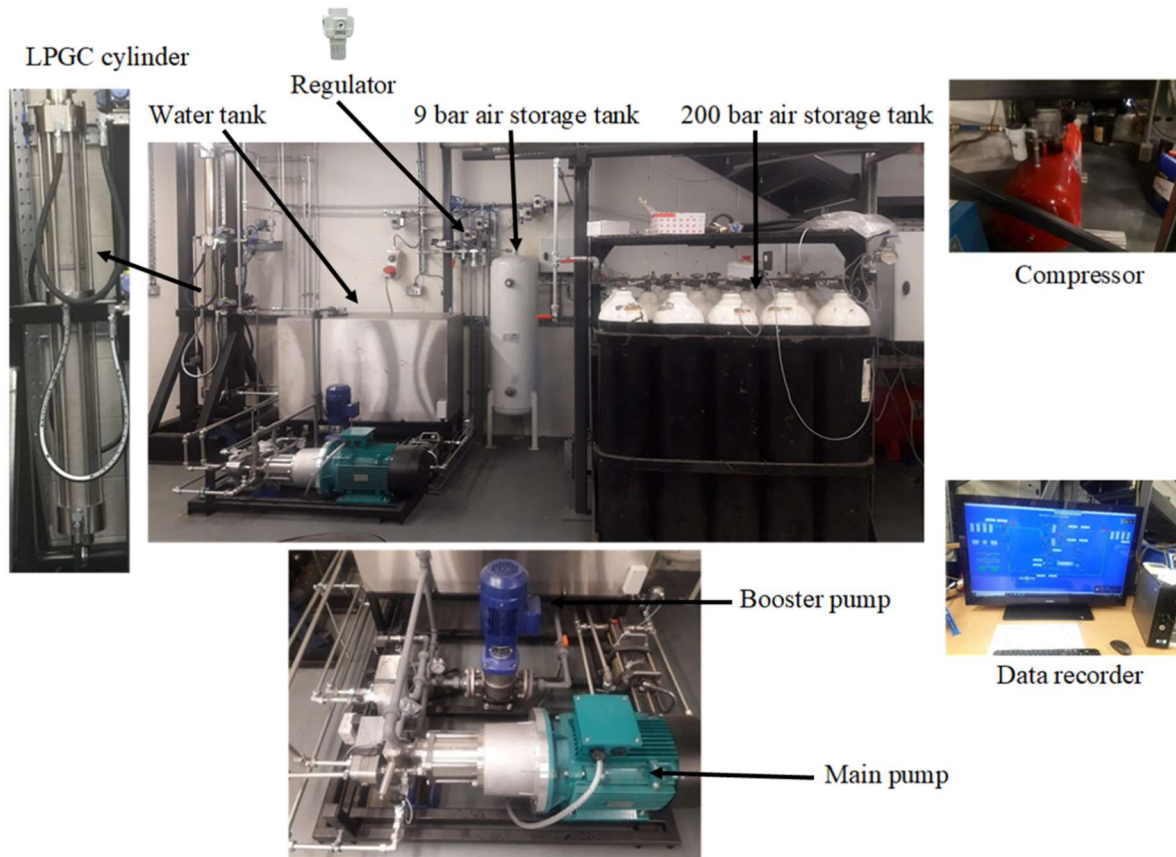
Figure 2. Experimental apparatus of a lab-scale CAES prototype system with a LPGC/E, motor power = 12 kW, volume of the air-storage tank = 0.7 m³.

4. Modelling methodology

The thermodynamic analysis of the proposed system detailed in this section is based on lumped mass and energy conservation equations written for each system component, assuming steady-state processes, except those involved in the LPGC/E. The LPGC/E works as a compressor when storing the compressed air during the charging stage and as an expander during discharge to produce electricity. As the LPGC/E is the main component of the CAES system and its performance has a significant effect on the performance of the system, the compression and expansion processes are modelled in transient conditions [35]. The air compressor is assumed adiabatic [36] and the air is assumed to be an ideal gas. It is also assumed that the CAES system operates under the rated condition, i.e., the load imposed on the system is assumed constant.

4.1 Transient mass and energy conservation for the LPGC/E

Figure 3 shows details of the heat exchange mechanisms between the air, water, LPGC/E cylinder walls and plates inside the LPGC/E cylinder.
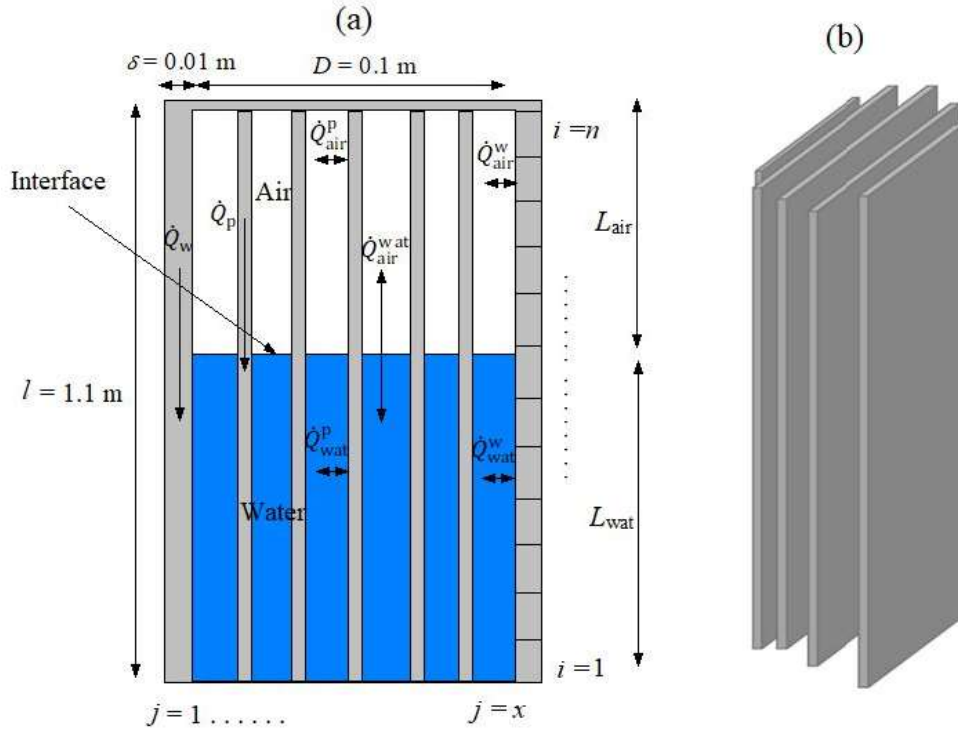

Figure 3. Schematic of compression chamber and heat transfer mechanisms between the air, water, cylinder wall and plates, and details of the arrangement of plates inside the chamber. $\dot{Q}^w_{air}$: Convection heat transfer from the air to the cylinder wall during compression or from the cylinder wall to the air during expansion. $\dot{Q}_w$: Conduction through the wall. $\dot{Q}^{wat}_{air}$: Conduction heat transfer from the air to the water during compression or from the water to the air during expansion. $\dot{Q}^w_{wat}$: Convection heat transfer from the water to the cylinder wall during compression or from the cylinder wall to the water during expansion. $\dot{Q}^p_{air}$: Convection heat transfer from the air to the plates during compression or from the plates to the air during expansion. $\dot{Q}^p_{wat}$: Convection heat transfer from the water to the plates during compression or from the plates to the water during expansion. $\dot{Q}_p$: Conduction through the plates.

The mass of air remains constant during the compression/expansion processes because the input air valve is closed. By considering the LPGC/E cylinder as the control volume, mass and energy balances are written for both the air and water phases:

$$m_{\text{air}} \frac{\mathrm{d}u_{\text{air}}}{\mathrm{d}t} = \dot{Q}_{\text{air}} - P \frac{\mathrm{d}V_{\text{air}}}{\mathrm{d}t}, \tag{1}$$

$$\frac{\mathrm{d}}{\mathrm{d}t} (m_{\text{wat}} u_{\text{wat}}) = \dot{Q}_{\text{wat}} - P \frac{\mathrm{d}V_{\text{wat}}}{\mathrm{d}t} \mp \frac{\mathrm{d}}{\mathrm{d}t} \sum \dot{m}_{\text{wat}} h_{in}, \tag{2}$$

where m_{air} is the total air mass inside the compression/expansion chamber, $\mathrm{d}u_{\text{air}}/\mathrm{d}t$ is the change in internal energy of air, $\dot{Q}_{\text{air}}$ is the total rate of heat transfer between air and the wall, plates and air and the water, and $P\mathrm{d}V/\mathrm{d}t$ is the rate of work which is done by water on the air during air compression process or the expansion work extracted by the air in the expansion process.

Since water is pumped into/blown out the compression/expansion chamber, the energy equation for an open system (control volume) is employed to the liquid, where $\mathrm{d}h_{in}/\mathrm{d}t$ is the enthalpy flow rate in/out the cylinder. Moreover, $\dot{Q}_{\text{wat}}$ is the total rate of heat transfer between water and the wall, plates and water and air, and m_{wat} is water mass, which can be calculated based on the constant mass flow rate as following:

$$\frac{\mathrm{d}m_{\text{wat}}}{\mathrm{d}t} = \mp \sum \dot{m}_{\text{wat}} \rightarrow m_{\text{wat}} - m_{\text{wat},0} = \mp \int_0^{t_{\text{comp/exp}}} \dot{m}_{\text{wat}} \mathrm{d}t, \tag{3}$$

where $m_{\text{wat},0}$ is the initial water mass occupied compression chamber.

Furthermore, $\dot{Q}_{\text{air}}$ and $\dot{Q}_{\text{wat}}$ in Eq. (1) and Eq. (2) can be written as:

$$\dot{Q}_{\text{air}} = \sum_{i=N}^{i=n} \left(\dot{Q}_{\text{air},i}^{\text{w}} \right) + \left(\dot{Q}_{\text{air},i}^{\text{p}} \right) + \dot{Q}_{\text{air}}^{\text{wat}}, \tag{4}$$

$$\dot{Q}_{\text{wat}} = \sum_{i=N}^{i=n} \left(\dot{Q}_{\text{wat},i}^{\text{w}} \right) + \left(\dot{Q}_{\text{wat},i}^{\text{p}} \right) + \dot{Q}_{\text{air}}^{\text{wat}}, \tag{5}$$

where $\dot{Q}^{\text{w}}_{\text{air},i}$ and $\dot{Q}^{\text{w}}_{\text{wat},i}$ are the air-to-wall and water-to-wall heat-transfer rates, respectively, $\dot{Q}^{\text{p}}_{\text{air},i}$ and $\dot{Q}^{\text{p}}_{\text{wat},i}$ are the air-to-plates and water-to-plates convective heat-transfer rates, respectively, and $\dot{Q}^{\text{wat}}_{\text{air}}$ is the rate of heat transfer between water and air, estimated as being a one-dimensional heat diffusion process, at each time step. In addition, n corresponds to the total discretisation number. In this equation, and for $\dot{Q}_{\text{wat}}$, the value of N is equal to 1 and n corresponds to the last node where water is in direct contact with the wall. For $\dot{Q}_{\text{air}}$, the value of N is equal to the node where the air is in direct contact with the water.

For the heat transfer analysis of the air compression/expansion process, it is assumed that the liquid levels in all ducts are the same. The hydraulic diameters of all ducts were considered as $D_{\text{h}} = 2L_{\text{z}}$ [37], where L_{z} is the distance between the parallel plates. Heat transfer exchange between the air and water through their interfaces is defined as [38]:

$$\dot{Q}_{\text{air}}^{\text{wat}} = U_{\text{int}}A_{\text{int}}(T_{\text{wat}} - T_{\text{air}}) \,, \tag{6}$$

$$U_{\text{int}}A_{\text{int}} = \frac{1}{\sum R_{\text{tot}}} = \frac{1}{\sum_{j=0}^{j=M}\left(\dfrac{L_{\text{wat}}}{k_{\text{wat}}A_j} + \dfrac{L_{\text{air}}}{k_{\text{air}}A_j}\right)} \,. \tag{7}$$

In Eq. (7), for the CAES$_{\text{plates}}$ configuration, j denotes the number of ducts (i.e., gaps between two parallel plates), which varies from $j = 0$ (for the baseline system configuration) to $j = M$, where x is the final number of ducts in the cylinder of this configuration, and A_j is the cross-sectional area of each duct. In the base-case configuration with no insert, A refers to the cross-sectional area of the cylinder, k is the thermal conductivity, and L is the height of water or air within the cylinder. Heat is transferred from the air to the parallel plates or cylinder wall by convection and conducted within the walls to the water. The heat transfer between the wall and water or air, and between the plates and water or air is modelled as [35]:

$$\dot{Q}_{\text{air},i}^{\text{w}} = \sum_{j=0}^{j=M} U_{\text{w},i,j}A_{\text{w},i,j}(T_{\text{w},i} - T_{\text{air}}) \,, \tag{8}$$

$$\dot{Q}_{\text{wat},i}^{\text{w}} = \sum_{j=0}^{j=M} U_{\text{w},i,j}A_{\text{w},i,j}(T_{\text{w},i} - T_{\text{wat}}) \,, \tag{9}$$

$$\dot{Q}_{\text{air},i}^{\text{p}} = \sum_{j=0}^{j=M} U_{\text{p},i,j}A_{\text{p},i,j}(T_{\text{p},i} - T_{\text{air}}) \,, \tag{10}$$

$$\dot{Q}_{\text{wat},i}^{\text{p}} = \sum_{j=0}^{j=M} U_{\text{p},i,j}A_{\text{p},i,j}(T_{\text{p},i} - T_{\text{wat}}) \,, \tag{11}$$

$$U_{\text{w},i,j}A_{\text{w},i,j} = \frac{1}{R_{\text{tot w},i,j}} \,, \tag{12}$$

$$R_{\text{tot w},i,j} = \frac{1}{\alpha_i A_{\text{w},i,j}} + \frac{\ln\left(\dfrac{\dfrac{D}{2} + \dfrac{\delta_{\text{w}}}{2}}{\dfrac{D}{2}}\right)}{2\pi L_{i,j}k_{\text{w}}} \,, \tag{13}$$

$$U_{\text{p},i,j}A_{\text{p},i,j} = \frac{1}{R_{\text{tot},\text{p},i,j}} \,, \tag{14}$$

$$R_{\text{tot},\text{p},i,j} = \frac{1}{\alpha_{i,j} A_{\text{p},i,j}} + \frac{\dfrac{\delta_{\text{p}}}{2}}{A_{\text{p},i,j}k_{\text{p}}} \,. \tag{15}$$

In the above equations, U is the overall heat transfer coefficient and R refers to heat transfer resistance of the wall or plates. In Eqs. (13) and (15), δ_{w} and δ_{p} are the thickness of the

cylinder wall and plates, respectively, and k is the thermal conductivity of the wall or plates. The heat conduction through the walls is modelled as:

$$\dot{Q}_{w,i} = \frac{k_w A_w \left(T_{w,i+1} - T_{w,i}\right)}{L_i}, \tag{16}$$

$$\dot{Q}_{p,i} = \sum_{j=1}^{j=M} k_p A_{p,j} (T_{p,i+1} - T_{p,i})/L_{i,j}, \tag{17}$$

$$\dot{Q}_{w,i} + \dot{Q}_{wat,i}^{w} = m_w c_{p,w} \left(\frac{dT_{w,i}}{dt}\right), \tag{18}$$

$$\dot{Q}_{w,i} + \dot{Q}_{air,i}^{w} = m_w c_{p,w} \left(\frac{dT_{w,i}}{dt}\right), \tag{19}$$

$$\dot{Q}_{p,i} + \dot{Q}_{air,i}^{p} = m_p c_{p,p} \left(\frac{dT_{p,i}}{dt}\right), \tag{20}$$

$$\dot{Q}_{p,i} + \dot{Q}_{wat,i}^{p} = m_p c_{p,p} \left(\frac{dT_{p,i}}{dt}\right). \tag{21}$$

In Eqs. (18) to (21), m and c_p are the mass and specific heat capacity of the wall or plate, respectively. In order to solve these equations, the convective heat transfer coefficient needs to be known. It can be calculated based on the flow regime, defined as Reynolds and Nusselt numbers. The general formulation of Nusselt number is as follows, where the coefficients vary with the flow regime and geometry of the container [38]:

$$Re_j = \frac{\rho v D_h}{\mu}, \tag{22}$$

$$D_h = \frac{4A}{P}. \tag{23}$$

In Eqs. (22) and (23), ρ and μ are the density and viscosity of air or water, respectively, and D_h, V, A and P are the hydraulic diameter, velocity, cross-sectional area and perimeter of each duct (j) or a circular cylinder for the base-case configuration. The Nusselt number for turbulent and laminar flow regimes is then calculated as [35, 38]:

$$Nu = C \, Re^a Pr^b \frac{\mu^c}{\mu_0}, \tag{24}$$

where C, a, b and c are constant parameters, and depend on the flow regime. For turbulent flow ($Re > 3000$) these coefficients are 0.02, 0.80, 0.30 and 0 for the water region [38], and 0.75, 0.80, 0.60 and 0 for the air region [35]. For the laminar flow regime ($Re < 2000$), these coefficients for air and water are taken to be 0.66, 0.50, 0.30 and 0, respectively [35]. In all cases, unsteady heat transfer (i.e., complex Nu) and associated losses are neglected [70].

The compression and expansion efficiencies are the key parameters used to evaluate the performance of a LPGC/E system. These efficiencies are defined as [21, 39]:

$$\eta_{\text{comp}} = \frac{E_s}{W_{\text{in}}}, \tag{25}$$

$$\eta_{\text{exp}} = \frac{W_{\text{out}}}{E_s}, \tag{26}$$

where E_s is the maximum energy storage for an isothermal expansion or compression of air in the LPGC cylinder. The stored energy is defined as follows [21]:

$$E_s = P_0 V_0 \ln|r_p|, \tag{27}$$

where V_0 and P_0 are the initial volume and pressure of the air in the cylinder, and r_p is the pressure ratio. Further, W_{in} in Eq. (25) is the compression work to compress air from an initial volume to a final volume for the desired pressure ratio and is defined as [21]:

$$W_{\text{in}} = (r_p P_0 - P_0) V_{\text{comp}} - \int_{V_0}^{V_{\text{comp}}} (P - P_0) \, dV. \tag{28}$$

and W_{out} in Eq. (26), is the expansion work from expanding air in the LPGC/E:

$$W_{\text{out}} = (r_p P_0 - P_0) V_{\text{comp}} + \int_{V_{\text{comp}}}^{V_{\text{exp}}} (P - P_0) \, dV. \tag{29}$$

where subscripts 'comp' and 'exp' refer to conditions at the end of the compression process and those at the at the final expansion pressure (see also Table 2).

In addition to efficiency, power density is also an important parameter for a LPGC/E system. The storage power of a compressor is defined as the ratio of the storage energy E_s to the compression duration t_{comp}. The power density of an expander is defined as the ratio of the output work (W_{out}) to the expansion duration t_{exp}. The compression/expansion power densities are the respective powers normalised by the compressor/expander volume, which consists of the expanded air volume V_0 and the solid volume of the porous insert V_{ins} [21]:

$$PD_{\text{comp}} = \frac{E_s}{t_{\text{comp}}(V_0 + V_{\text{ins}})}, \tag{30}$$

$$PD_{\text{exp}} = \frac{W_{\text{out}}}{t_{\text{exp}}(V_0 + V_{\text{ins}})}. \tag{31}$$

4.2 Quasi-steady description of remaining components

The thermodynamic relations for all other system components are given in Table 1, and it is assumed the inertial terms (dynamics) of all other components are fast and can be neglected.

Table 1. Energy balance relations for the components of the CAES system [35, 40, 41].

Component	Energy balance equation
Compressor	$\eta_{\text{comp,9bar}} = (h_{\text{out,s}} - h_{\text{in}})/(h_{\text{out}} - h_{\text{in}})$ and $\dot{W}_{\text{comp,9bar}} = \dot{m}_{\text{air}}(h_{\text{out}} - h_{\text{in}})$
Pump	$\eta_{\text{pump}} = ((r_{\text{p}}P_0 - P_0)V_{\text{comp}} - \int_{V_0}^{V_{\text{comp}}}(P - P_0)\,\mathrm{d}V)/\dot{W}_{\text{in,pump}}$
Regulator	$h_{\text{out}} = h_{\text{in}}$
Air-storage tanks	$p_{\text{in}} = p_{\text{out}}$ and $\dot{Q}_{\text{AST}} = \dot{m}_{\text{air}}(h_{\text{in}} - h_{\text{out}})$
Valves	$h_{\text{in}} = h_{\text{out}}$
PCM heat exchanger	$\dot{Q}_{\text{HX,chg}} = \dot{m}_{\text{air}}(h_{\text{out}} - h_{\text{in}}) = U_{\text{HX}}A_{\text{HX}}\Delta T_{\text{LMTD}}; \dot{Q}_{\text{HX,dchg}} = \dot{m}_{\text{air}}(h_{\text{out}} - h_{\text{in}})$ $\eta_{\text{HX}} = \frac{\dot{Q}_{\text{HX,dchg}}t_{\text{dchg}}}{\dot{Q}_{\text{HX,chg}}t_{\text{chg}}}; \Delta T_{\text{LMTD}} = \frac{\Delta T_1 - \Delta T_2}{\ln\frac{\Delta T_1}{\Delta T_2}}$
Heater	$\dot{Q}_{\text{htr}} = \dot{m}_{\text{air}}(h_{\text{out}} - h_{\text{in}})$

In the above equations, ΔT_1 and ΔT_2 are the temperature differences between the hot and cold fluids in the two hot and cold air streams in the PCM heat exchanger. Further, t_{chg} and t_{dchg} are used to denote the time associated with the charging and discharging processes of the storage tank and depend on the mass flow rate of the air, the volume of the storage tank and the pressure of the air, which can be determined from [42, 43]:

$$V_{\text{AST}} = \frac{\dot{m}_{\text{chg}}t_{\text{chg}}R_{\text{g}}\gamma T_{\text{in}}}{(P_{\text{in}} - P_0)} \,, \tag{32}$$

$$\frac{t_{\text{chg}}}{t_{\text{dchg}}} = \frac{\dot{m}_{\text{chg}}}{\dot{m}_{\text{dchg}}} \,, \tag{33}$$

where γ and R_{g} are the specific heat ratio of the air and ideal gas constant, respectively, T_{in} and P_{in} are the inlet temperature and pressure of the air as this flows into the air-storage tank, and P_0 is the initial pressure of the air inside the tank at the start of the charge process (and the final air pressure at the end of the discharge process). In this work, t_{chg} is considered to be 3.5 h. The storage volumes for each configuration and t_{chg} are determined Eqs. (32) and (33), respectively. It is noted that this is the minimum size of storage tank for a given air quantity and pressure, and thus corresponds to the smallest (minimum limiting) cost associated with this component.

It should be noted that when modelling the operation of the CAES$_{base}$, CAES$_{plate}$ and CAES$_{heater}$ configurations, the high-pressure air is assumed to cool down to ambient temperature prior to and during this being stored in the 200-bar air-storage tank(s). For the CAES$_{PCM}$ and CAES$_{PCM\&plate}$ configurations, the high-pressure air stored in the tank is assumed to cool down fully to ambient temperature in a heat-rejection process that also reduces the pressure of the air in the storage tank, however, this pressure drop is small. For the modelling of the discharge process in all configurations, it is assumed that the storage tank is large enough such that the air maintains a constant pressure (200 bar) for the duration of this process [44].

The EES environment is used to solve the governing equations described above using the input parameters provided in Table 2.

Table 2. Input parameters used in thermodynamic modelling [40, 41, 45, 46].

Parameter	Value
P_0, T_0	1 bar, 298.15 K
Compression ratio in 9 bar compressor	9
$\eta_{comp,9bar}$	88%
η_{pump}	96%
η_{gen}	96%
$P_{in,LPGC/E}$	8 bar
Compression ratio in LPGC/E	25 (8-200 bar)
Expansion ratio in LPGC/E	100 (200-2 bar)
Inner diameter of LPGC/E cylinder	0.1 m
Height of cylinder	1.1 m
Height of the parallel plates inside cylinder	1.1 m
Thickness of plates	0.001 m
Thickness of cylinder	0.01 m
Distance between plates	0.016 m
Number of plates	5

4.3 Modelling of PCM heat exchanger

PCMs are substances that release/absorb sufficient energy at phase transition to provide useful heating or cooling. PCMs are found in different applications due to their thermal characteristics, such as in building envelope, industry thermal energy storage (TES), battery thermal

management and electric/power peak regulation [47]. In the present work, for CAES$_{PCM\&plate}$ configuration, a PCM material is used in the heat exchanger to absorb the thermal energy of the hot compressed air during the charging process. Then, the stored thermal energy is used to preheat the compressed air during the discharge process, before expanding in the LPGC. A tube PCM heat exchanger is considered to store and release the thermal energy of the compressed air [48]. Figure 4 illustrates the schematic of the PCM heat exchanger. The system consists of a PCM with mass m. Air with mass flow rate $\dot{m}$ flows inside the smaller diameter tube where it exchanges heat with the PCM. Through the charging process, the PCM changes phase from solid to liquid, while during the discharging process, the PCM changes phase from liquid to solid. The phase change takes place at a constant melting temperature [49].
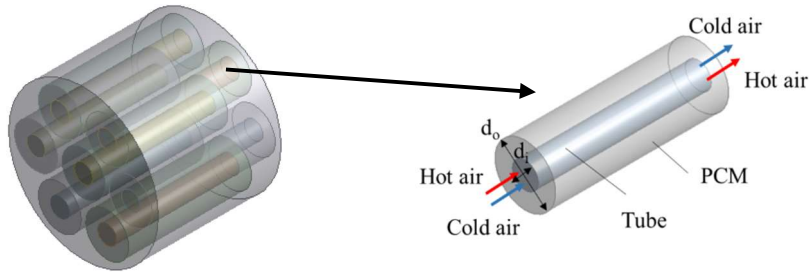

Figure 4. Schematic of the PCM heat exchanger analysed in this work.

The PCM is selected based on the final temperature of the compressed air at the end of the compression (charging) and the desired air temperature before expansion (discharging). In this regard high temperature molten salts (H160 and H105 in Ref. [48]) are used as the PCM for CAES$_{PCM}$ and CAES$_{PCM\&plates}$ configurations, respectively. The thermal properties of the PCM and the parameters considered for modelling of the heat exchanger are summarised in Table 3 [50]. The heat transfer surface area is needed to calculate the cost of the PCM heat exchanger for the technoeconomic analysis. To calculate the heat transfer surface area, the overall heat transfer coefficient between the air and the PCM must be determined from Eq. (34). The calculation of the overall heat transfer coefficient between the air and the PCM is described below. The general equation of heat transfer from a surface is defined as follows [41, 51, 52]:

$$Q = UA\Delta T_{\mathrm{LMTD}} , \qquad (34)$$

where Q is heat transfer rate, U is the overall heat transfer coefficient, A is the heat transfer area, and ΔT_{LMTD} is the logarithmic mean temperature difference.

The overall heat transfer coefficient, U, in Eq. (34), is calculated from:

$$1/U = 1/\alpha_o + d_o \ln(d_o/d_i)/2k_w + d_o/d_i \times 1/\alpha_i , \qquad (35)$$

where α_o and α_i are the PCM and air convective heat transfer coefficients, respectively, k_w is the thermal conductivity of the tube wall material, and d_o and d_i are the outer and inner diameters of the tubes in the PCM heat exchanger. The air heat transfer coefficient α_i, in Eq. (35), is determined from one of the following well-known correlations [49]:

$$\text{Laminar flow: } \alpha_i d_i/k_f = 3.66 , \qquad (36)$$

$$\text{Turbulent flow: } \alpha_i d_i/k_f = 0.023 Re^{0.8} Pr^n , \qquad (37)$$

where k_f is the air thermal conductivity, which is calculated at the average temperature between the inlet and the outlet conditions of the tube, Re and Pr are the Reynolds number and the Prandtl number of the air in the tube, respectively, with parameter n set to 0.4 for the discharging process and $n = 0.3$ for the charging process [49]. The heat transfer coefficient between the wall and the PCM, α_o, is also obtained using known correlations [53]:

$$\text{Solidification process: } \alpha_o = 2 k_{PCM}/[0.4 d_i \ln(d_o/d_i)] , \qquad (38)$$

$$\text{Melting process: } \alpha_o = Nu k_f/\delta_{PCM} , \qquad (39)$$

where Nu is the Nusselt number, δ_{PCM} is the thickness of the PCM material that is $(d_o - d_i)/2$ and l is the heat exchanger length. For $\delta_{PCM} \leq 6$ mm, natural convection heat transfer does not occur in a form associated with a thin liquid layer, and the heat is transferred only by heat conduction. In this case, Nu in Eq. (38) is evaluated from the following relations [49]:

$$Nu = 1 \text{ for } Re < 10^3 , \qquad (40)$$

$$Nu = 0.028 \, Re^{1/4}(l/\delta_{PCM})^{-1/4} \text{ for } 10^3 < Re < 10^7 . \qquad (41)$$

On the other hand, when $\delta_{PCM} > 6$ mm, the heat transfers between the liquid and PCM is accrued by natural convection and the following equation is used to estimate Nu:

$$Nu = 0.133 \, Re^{0.326}(l/\delta_{PCM})^{-0.0686} . \qquad (42)$$

Table 3. Thermal properties of H160 and H105 as the PCMs and the parameters considered for modelling of the PCM heat exchanger [50].

Item	Value for H160	Value for H105
Melting temperature	435 K	377 K
Enthalpy fusion	105 kJ/kg	125 kJ/kg
Specific heat capacity of PCM	1505 J/kgK	1500 J/kgK

Conductivity of solid PCM	0.50 W/mK	0.50 W/mK
Outer diameter (d_o) of tube	20 mm	20 mm
Inlet diameter (d_i) of tube	16 mm	16 mm
Thermal conductivity of the wall (k_w)	50 W/mK	50 W/mK

4.4 Technoeconomic analysis

To further assess the feasibility of the proposed CAES systems, it is imperative to analyse the systems from an economic perspective. An important factor for assessing a system economic viability is the policy and financial instruments in place within the country that may benefit the system implementation [54]. This includes looking at subsides and tariffs. In the UK, the smart export guarantee (SEG) scheme can apply to the proposed energy storage systems. The SEG scheme pays a dividend to those that generate electricity and feed it into the national grid. The SEG grant is based on the electricity fed to the grid. The SEG changes between electricity providers which the SEG value of 5.5 p/kWh (6.8 ¢/kWh) is used at the present work [54].

Further, the system is analysed in terms of the annual total cost (ATC), annual total income (ATI), annual total profit (ATP), total investment cost (TIC), operation and maintenance costs ($C_{O\&M}$) and dynamic payback period (DPP). The ATC mainly consists of annual $C_{O\&M}$ and running cost due to electricity or fuel C_{in} [55], which is defined as:

$$ATC = C_{O\&M} + C_{in} .$$ (43)

The operation and maintenance cost $C_{O\&M}$ for large scale CAES is considered as 0.003 \$/kWh, and is very low for small-scales CAES systems [56]. However, the reversible pump is expected to be the main component in the system, which would require annual maintenance. Therefore, the operation and maintenance cost of the reversible pump (113 \$/year) is considered as $C_{O\&M}$ in this work [57].

The investment costs of the system components were also estimated in order to calculate the investment payback periods. The total investment cost of the components is calculated from:

$$TIC = \sum_i PEC_i ,$$ (44)

where PEC_i is the investment cost of the system components determined using the functions provided in Table 4 for the compressor, heater and heat exchanger taken from Ref. [58]. It is worth mentioning that the LPGC/E cylinder, regulator, reversible pump, air and water storage tanks, parallel plate inserts and valve costs are based on purchase orders from suppliers, and that

all costs correspond a unique unit for demonstration purposes. It is expected that by developing the proposed system, the overall investment cost will be reduced thanks to economies of scale.

Table 4. Purchase equipment cost (*PEC*) of the CAES system components [58, 59].

Component	Cost function [$]	Material/parameter	Price
Compressor	$PEC_{\text{comp,9bar}} = 1.81(\dot{W}_{\text{comp}}/0.74)^{0.71}$	-	$1220
Regulator	28	-	$28
9-bar air-storage tank	450	-	$450
200-bar air-storage tank	$2284-3462*	Stainless steel	$2350
Valve	4 × $433	Relief valve	$1730
LPGC/E$_{\text{comp/exp}}$	$2700	Stainless steel	$2700
Reversible pump	4340	Stainless steel	$4340
PCM heat exchanger (HX)	$PEC_{\text{HX}} = 130\left(\dfrac{A_{\text{HX}}}{0.093}\right)^{0.78} + PEC_{\text{PCM}}$	-	$2300
Water tank	178	250-L GRP tank	$178
Parallel plates	50	Aluminium	$50
Heater	$PEC_{\text{htr}} = 1.22 f_{\text{m}}(1 + f_{\text{d}} + f_{\text{p}})(\dot{Q}_{\text{htr}})^{0.86}$	f_{m}=25.5, f_{d}=0, f_{p}=0.6	$200

* This price is for two packs of pallets each with 16 cylinders which were used in the experiment for the CAES$_{\text{base}}$ configuration (each cylinder has a volume of 0.044 m^3). For other configurations, different tank volumes and hence different prices are considered. Both t_{chg} and t_{dchg} are constant for all CAES configurations. Therefore, the price for the air-storage tank in each configuration is calculated based on the required volume to store compressed air in each configuration. For CAES$_{\text{base}}$, CAES$_{\text{plate}}$, CAES$_{\text{PCM}}$ and CAES$_{\text{PCM\&plate}}$, the tank volumes are given in Table 9, with corresponding tank prices of $3460, $2780, $2630 and $2280, respectively.

The costs of the compressor and heat exchangers are based on purchase costs in 2009 [58]. The cost of the LPGC/E, regulator, air and water storage tanks, reversible pump and valves are based on suppliers' receipts in 2019. Hence, Eq. (45) is used to convert the costs of purchasing all equipment from the base year 2009 to the reference year (2019) [36, 41]:

$$PEC_{\text{ref,y}} = PEC_{\text{base,y}} \times (CI_{\text{ref,y}}/CI_{\text{base,y}}), \tag{45}$$

where CI is the cost index calculated based on the Marshal and Swift index used in Ref. [60].

The annual input cost is the peak-off electricity cost at charging time. Considering the electricity price distinction between the on-peak hour and off-peak hour, the charging process and discharging process are assumed to be separated. Therefore, the actual operating hour in one day is the sum of charging time and discharging time. The annual input cost is then [55]:

$$C_{\text{in}} = (t_{\text{chg}} \times \dot{W}_{\text{in}} \times C_{\text{off-peak}} \times 365) + t_{\text{dchg}} \times \dot{m}_{\text{fuel}} \times C_{\text{fuel}} \times 365 , \qquad (46)$$

where $\dot{W}_{\text{in}}$ is the electricity consumed by the compressor and pump during the charging process (kW), $C_{\text{off-peak}}$ the electricity price during the off-peak hour ($/kWh), and $\dot{m}_{\text{fuel}}$ the amount of natural gas needed to be used in the heater for the CAES$_{\text{heater}}$ configuration in Figure 1. The annual total income (ATI) consists of net output electricity income:

$$ATI = t_{\text{dchg}} \times \dot{W}_{\text{out}} \times C_{\text{on-peak}} \times 365 , \qquad (47)$$

where $\dot{W}_{\text{out}}$ is the net output electricity of the system (kW), and $C_{\text{on-pe}}$ the electricity price during on-peak hours ($/kWh). The annual total profit (ATP) of the proposed system is then:

$$ATP = ATI - ATC . \qquad (48)$$

The equations above along with the economic parameters given in Table 5 are solved in EES to analyse the economic performance of the different CAES system configurations in Section 2.

Table 5. Related economic parameters of proposed systems.

Parameter	Value
Economic life of CAES with LPGC/E	20 years
Cost of electricity	Off-peak = 7.46 p/kWh*; On-peak = 29.75 p/kWh* [61]
Cost of fuel (natural gas)	0.796 $/L [62]
Discount rate (r_{d})	3% [63]
Inflation rate (r_{i})	3% [64]

* Note: 1 $ (USD) = 80.4 pence (p), 1 GBP = 100 pence (p) and 1 $ = 100 cent (¢).

Finally, it is desired to estimate the emission reduction and fuel savings with the installation of the CAES systems. This is done by comparing the above proposed systems with those from a conventional power plant fuelled by natural gas which provides electricity to the grid. In addition, the amount of CO_2 emission and fuel consumption in the heater of CAES$_{\text{heater}}$ configuration are calculated based on CO_2 factor and fuel consumption factor for the heat. The CO_2 emission factor and fuel consumption factor for the heater in the configuration of CAES$_{\text{heater}}$ is considered as 0.18 kg CO_2/kWh$_{\text{th}}$ and 0.25 kg/kWh$_{\text{th}}$, respectively. Under the UK's climate change agreements (CCAs) (Environment Agency, 2019), it is assumed that twice as many units of fuel are required to generate each unit of electricity than are required to generate each unit of heat. Therefore, the conventional power

plant is assumed to burn around 0.5 kg of natural gas and emits around 0.36 kg per kWh of electricity [65]. Thus, the proposed CAES systems should have a significant effect in reducing the environmental impact of energy consumption, by reducing fuel consumption, enabling renewable uptake and reducing emissions. Clearly, the development of such energy storage systems has a very significant role to play in contributing towards the increasingly stringent emission and renewable energy targets of UK, but also of the EU and globally [66].

4.5 Performance criteria and objective functions

To evaluate the operational characteristics of the proposed CAES systems, some evaluation indicators are needed to compare the performances of the systems. Considering the distinctions of time between charging and discharging process, the inputs and outputs should also consider the time effect. These indicators are explained in the following sub-sections.

4.5.1 Roundtrip efficiency

To reflect the time difference between the air compression and expansion, the energy efficiency based on charging time and discharging time is presented. The roundtrip efficiency is defined as the ratio of output energy to input energy in a full charging and discharging cycle as [59]:

$$\eta = \frac{t_{\mathrm{dchg}} \times \dot{W}_{\mathrm{out,gen}}}{t_{\mathrm{chg}} \times \left(\dot{W}_{\mathrm{pump}} + \dot{W}_{\mathrm{comp,9bar}}\right) + t_{\mathrm{dchg}} \times \dot{Q}_{\mathrm{htr}}}, \qquad (49)$$

where $\dot{W}_{\mathrm{out,gen}}$ is the net output electricity from the generator, $\dot{W}_{\mathrm{in}}$ is the electricity consumption of the 9-bar air compressor and the water pump, and $\dot{Q}_{\mathrm{htr}}$ is the required heat by the heater to preheat the compressed air before expansion.

4.5.2 Charging efficiency

The charging electricity efficiency is defined as the ratio of power generated by the expander to the input energy of the CAES system, which can be expressed as:

$$\eta_{\mathrm{CEE}} = \frac{t_{\mathrm{dchg}} \times \dot{W}_{\mathrm{exp,LPGC}}}{t_{\mathrm{chg}} \times \left(\dot{W}_{\mathrm{comp,LPGC}} + \dot{W}_{\mathrm{comp,9bar}}\right) + t_{\mathrm{dchg}} \times \dot{Q}_{\mathrm{htr}}}. \qquad (50)$$

where $\dot{W}_{\mathrm{exp,LPGC}}$ is the power generated by the LPGC/E and $\dot{W}_{\mathrm{comp,LPGC}}$ is the required power to compress the air from 8 bar to 200 bar.

4.5.3 Dynamic payback period

The payback period is the time required for the system to recover its initial investment cost. The dynamic payback period (DPP) mainly considers the time value, which is calculated when the cumulative net present value (NPV) is zero [57] and expressed as:

$$DPP = \lfloor DPP - 1 \rfloor + \frac{\left| NPV_{\lfloor DPP-1 \rfloor} \right|}{ATP_{\lfloor DPP \rfloor}}, \tag{51}$$

where $ATP_{\lfloor DPP \rfloor}$ is the cash flow in year $\lfloor DPP \rfloor$, and $\left| NPV_{\lfloor DPP-1 \rfloor} \right|$ is the absolute value of NPV until the year $\lfloor DPP - 1 \rfloor$. The net present value (NPV) is the difference between the present value of cash inflows and outflows during a period, which mainly presents the balance between the present value of total income and initial investment, and is expressed as:

$$NPV = \sum_{y=1}^{n} \frac{ATP_y \, (1 + r_i)^y}{(1 + r_d)^y} - TIC, \tag{52}$$

where r_d is the discount rate of 3%, r_i is the inflation rate of 3% as given in Table 5, ATP_y is the cash flow in year y, and TIC is the total investment cost. The inflation rate r_i (referring to the consumer price index, CPI) in the UK is expected to vary, and historical values show a wide range of rates form -0.1% to 5.2%. An average value of 3% is considered in this study [64].

5. Results and discussion

5.1 Experimental data analysis of charging process and model validation

In this section, the results of the thermodynamic model are compared with experimental data for the compression process in the base-case configuration (CAES$_{base}$). Air is compressed from 8 bar to 40 bar in the LPGC/E and stored in the storage tank. In the experiments, temperature and pressure data are obtained for the air and water at different locations in the systems (including States 2, 5, 6, 8 and 12 in Figure 1(a)). The predictions of the present thermodynamic models are compared against the experimental data and the results are shown in Table 6. It is seen that the model predicts well the pressure and temperature data at the different locations of the CAES testbed, with maximum relative errors below 7%.

Table 6. Model validation against experimental data for the base-case CAES system, CAES$_{base}$.

State	Working fluid	Model		Experimental data		Error (%)	
		T (K)	P (bar)	T (K)	P (bar)	T (%)	P (%)
4	Air	298	9.0	299	8.5	0.2	5.5
5	Air	298	8.0	299	7.5	0.2	6.2
6	Air	473	40.0	470	41.0	0.6	2.5
8	Water	298	1.0	297	1.2	-0.4	2.0
12	Water	300	1.0	301	1.3	0.3	3.0

Furthermore, the transient model developed for the LPGC/E is validated in detail against the experimental data collected from our experimental testbed when the air is compressed from 8 bar to 40 bar. Each test was repeated at least for ten times and the data was collected for three different compression durations (water flow rate). The water flow rate for compression versus compression duration is shown in Figure 5. The water flow rate changes from 30 L/min for 3.5 s to 50 L/min for 1.7 s. Figure 5 shows that the highest water flow rate of 50 L/min leads to the fast compression which occurs in 1.7 s. While, with the water flow rate of 40 L/min and 30 L/min, it takes 2.5 s and 3.5 s, respectively compress the air from 8 bar to 40 bar. In slower compression, a slight fluctuation is seen in the water flow rate. When compression starts, the mass flow rate of the water increases and at the end of compression, it drops to the initial value. It worth mentioning that the mass flow rate of the water never drops to zero at the end of compression because two LPGC/Es work in parallel, continuously.

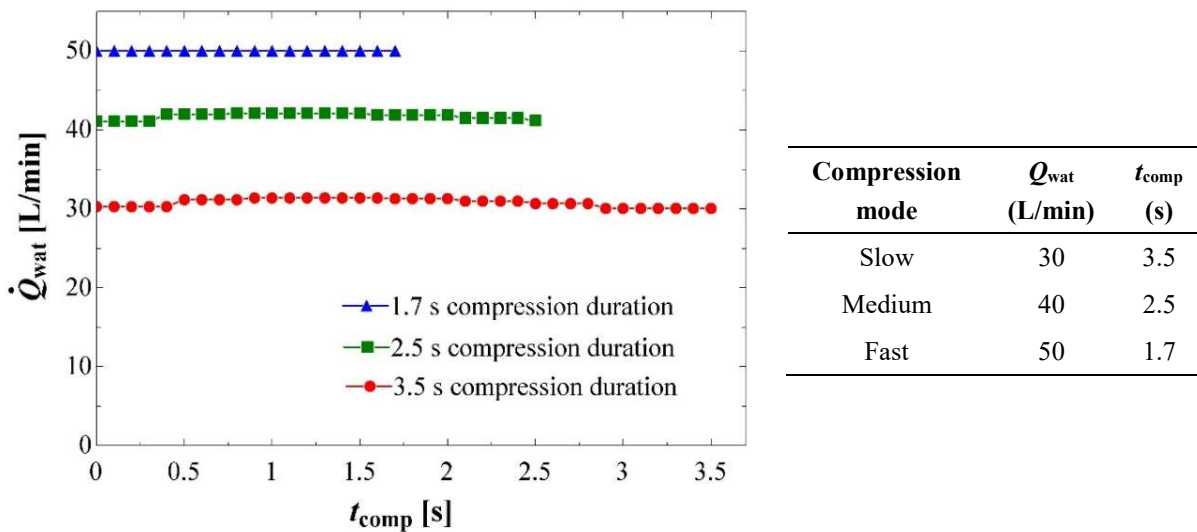| Compression mode	Q_{wat} (L/min)	t_{comp} (s)
Slow	30	3.5
Medium	40	2.5
Fast	50	1.7

Figure 5. Compression water flow rate as a function of compression duration with an initial pressure

of 8 bar, a final pressure of 40 bar, and water flow rates of 50 L/min, 40 L/min and 30 L/min corresponding to compression durations of 1.7 s, 2.5 s and 3.5 s.

Figure 6 shows pressure-volume curves derived from experimental data for the LPGC/E in the base-case configuration CAES$_{base}$. This suggests that for the slow compression (water flow rate of 30 L/min) the area under P-V is lower than that in the fast compression (water flow rate of 50 L/min), so the slow compression gives more time to transfer heat from the compressed air to the cylinder wall and water, supporting a near-isothermal compression process.
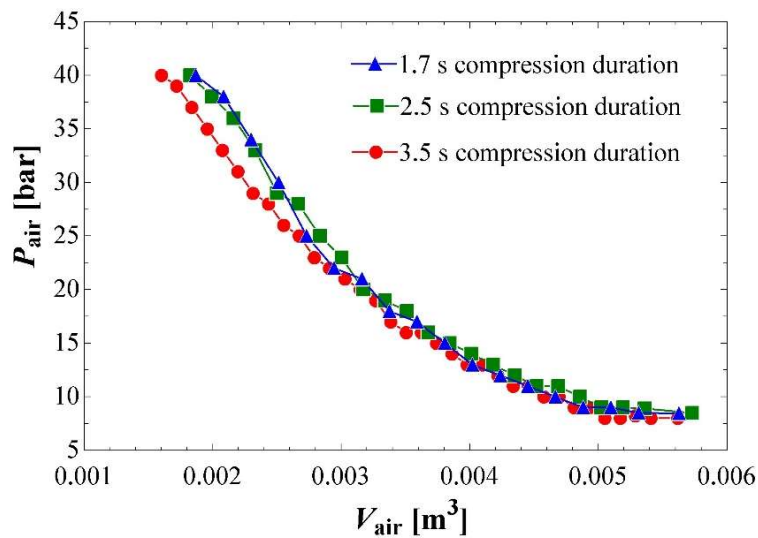

Figure 6. Pressure-volume traces during compression at various motor speeds for the LPGC/E base-case configuration CAES$_{base}$ with an initial pressure of 8 bar, a final pressure of 40 bar, and water flow rates of 50 L/min, 40 L/min and 30 L/min corresponding to compression durations of 1.7 s, 2.5 s and 3.5 s, respectively.

For each test reported in Figure 6, the compression efficiency is plotted against its power density in Figure 7. Increasing the power density corresponds with higher compression rates and shorter compression durations. It can be seen that there is a relationship between efficiency and power density, with any increase in power density accompanied by a decrease in efficiency. There is a good agreement between the model predictions of compression efficiency versus power density (Figure 7) and the experimental results, with around a 2.5% difference.
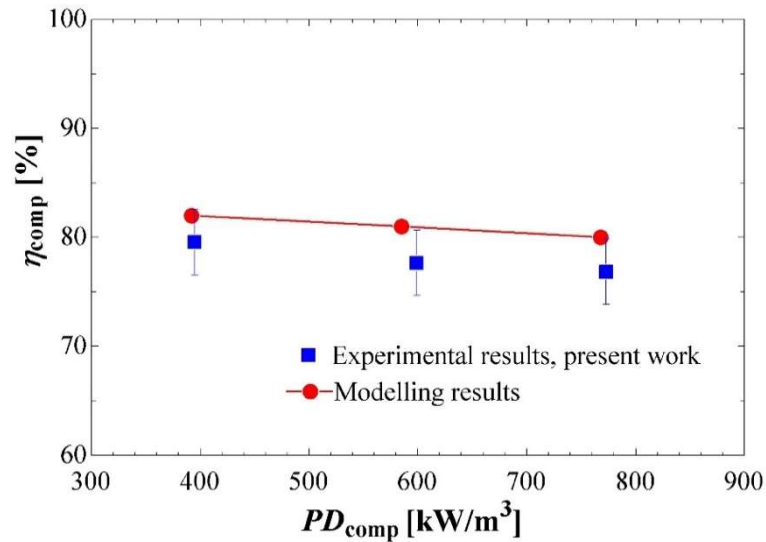
Figure 7. Validation of the LPGC/E transient model in the compression phase for the base-case configuration CAES$_{base}$ against experimental data, with an initial pressure of 8 bar, a final pressure of 40 bar, and power densities from 400 kW/m^3 to 800 kW/m^3 corresponding to water flow rates from 30 L/min to 50 L/min and compression durations from 3.5 s to 1.7 s.

The expansion process model may also be validated against data in the literature [22]. In a further validation analysis, the LPGC/E dimensions were matched to those in Ref. [22], with the air expanded from 10 bar to 1 bar. Figure 8 illustrates the expansion efficiency of the LPGC/E as a function of power density. It is seen that the model predicts the experimental data well.
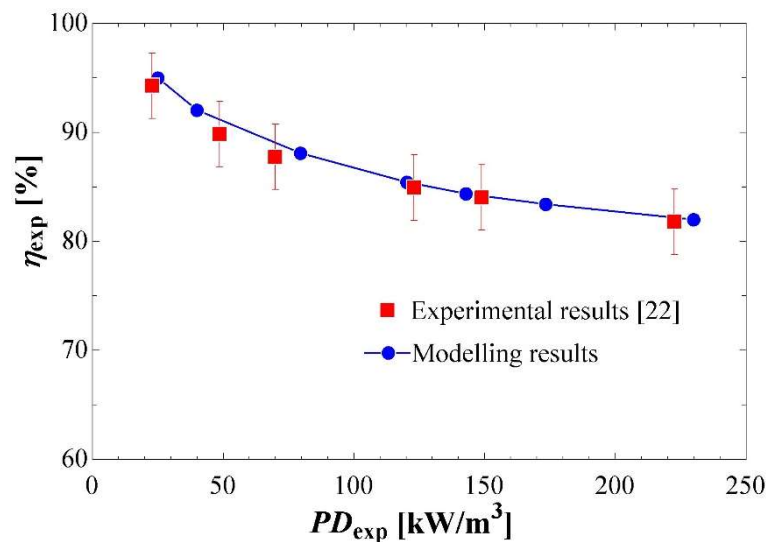

Figure 8. Validation of the LPGC/E transient model in the expansion phase for the base-case

configuration CAES_base against experimental data [22] for an initial pressure of 10 bar. A final pressure of 2 bar, and power densities from 20 kW/m^3 to 240 kW/m^3.

5.2. Modelling of cyclic system operation

Using the thermodynamic model validated in the previous section, the time-dependent air thermophysical properties in the LPGC/E are predicted for a compression from 8 to 200 bar and expansion from 200 down to 2 bar [22]. Figure 9 shows temperature-volume diagrams generated during the air compression phase with different compression durations with no inserts. For low compression duration (faster compression), the *T-V* diagram tends closer to adiabatic compression, while for higher compression duration (slower compression), the diagrams become more isothermal. This is because in the fast compression case, there is not enough time to transfer heat from the hot air to the cylinder wall or water, while in the slower compression case the air has enough time to transfer the heat to the environment, hence the air is compressed near-isothermally.

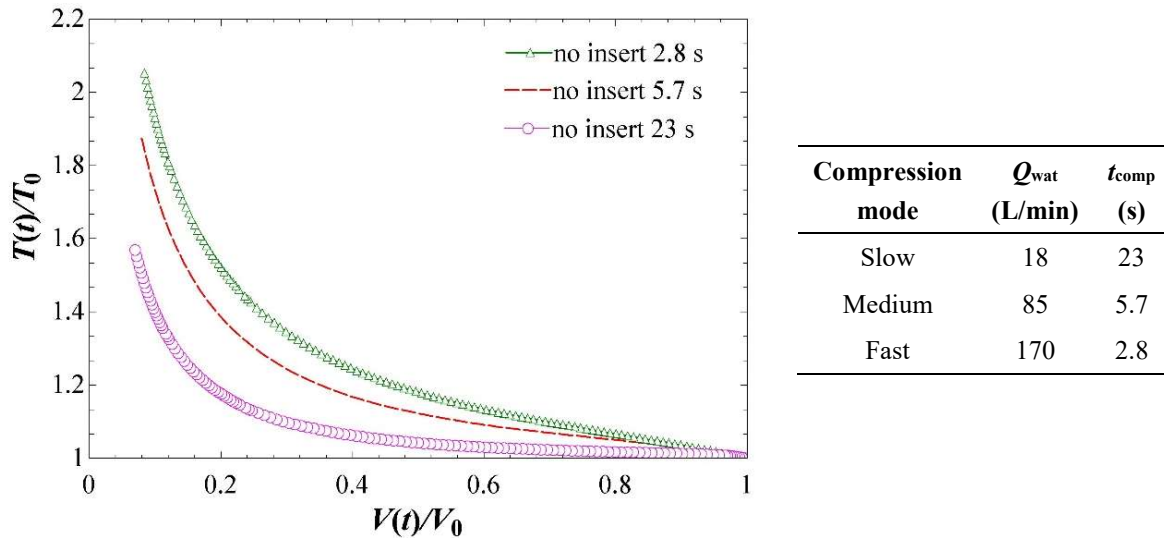| Compression mode	Q_{wat} (L/min)	t_{comp} (s)
Slow	18	23
Medium	85	5.7
Fast	170	2.8

Figure 9. Temperature-volume diagrams for the LPGC/E with no parallel-plate insert at various compression durations of 2.8 s, 5.7 s, and 23 s corresponding to water flow rates of 170 L/min, 85 L/min and 18 L/min, respectively.

Temperature-volume (*T-V*) diagrams for the expansion process without inserts are shown in Figure 10. It is seen that for each expansion duration, the air temperature tends to decrease rapidly initially to a minimum temperature and subsequently increases towards a temperature,

which is slightly lower than the initial temperature. This non-monotonic behaviour was observed in the experimental work done by Wieberdink et al. [23]. It is due to power levels towards the latter part of the expansion (lower pressure and larger volume) being lower than the heat transfer rate, which is facilitated by an established temperature difference and increasing surface area for heat transfer rate. For the fastest expansion (0.75 s), the temperature drops down as low as 125 K (i.e., $T/T_0 = 0.42$), while, for the slowest expansion (6.0 s), the air temperature drops to a value of 175 K (i.e., $T/T_0 = 0.58$). In comparison to the fast expansion, the air temperature at the end of the expansion process is closer to the initial temperature.
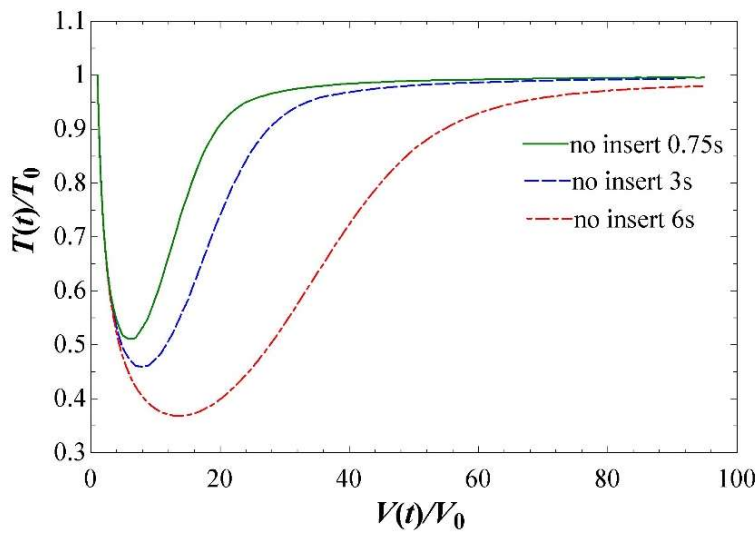

Expansion mode	Q_{wat} (L/min)	t_{exp} (s)
Slow	85	6
Medium	170	3
Fast	660	0.75

Figure 10. Temperature-volume diagrams for the expansion process for the LPGC/E with no parallel-plate insert at expansion durations of 0.75 s, 3 s, and 6 s corresponding to water flow rates of 660 L/min, 170 L/min and 85 L/min, respectively.

Efficiencies and power densities of the LPGC/E are obtained using Eqs. (20), (21), (25) and (26). The efficiency is plotted against its power density in Figure 11 for compression and expansion processes, respectively. Increasing power density corresponds to a higher compression/expansion rate and shorter time. For both cases (baseline and parallel plate insert), there is a trade-off between efficiency and power density; an increase in the power density results in a decrease in compression or expansion efficiency. For similar compression/expansion efficiencies, the insert case shows higher power density than the baseline case. Additionally, for the same power density, the insert case exhibits a higher efficiency than the base-case configuration. For instance, in compression process and at 200 kW/m^3 power density, the

compression efficiency is increased by 4% from 80% to 86%. For expansion process and at 200 kW/m^3 power density, parallel-plate inserts increase the efficiency by 12% from 72% to 84%. Such increases in efficiency are due to the near-isothermal compression/expansion processes occur in the LPGC/E, resulting from a higher air-to-plate heat transfer rates.

In this section, the physical behaviour of the air explained in the compression and expansion phases with no insert and with insert. In the following section, the performance of the whole system is analysed by considering the compression duration as 5.7 s and expansion duration as 3 s, in order to select the most cost-effective CAES system.
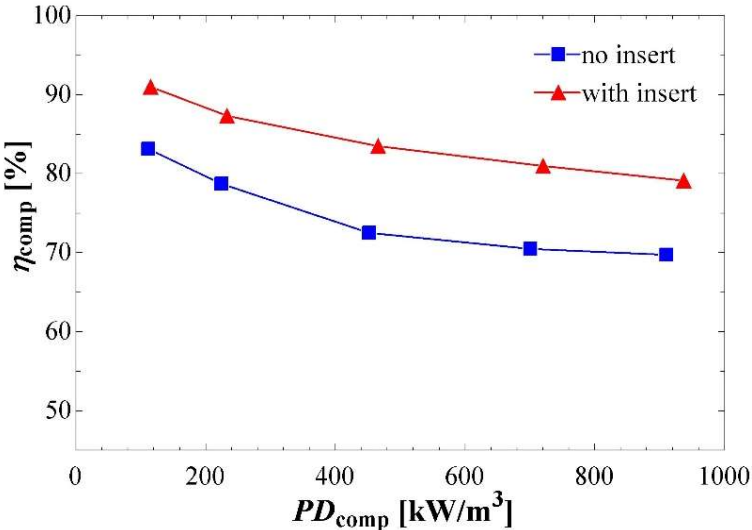
(a)
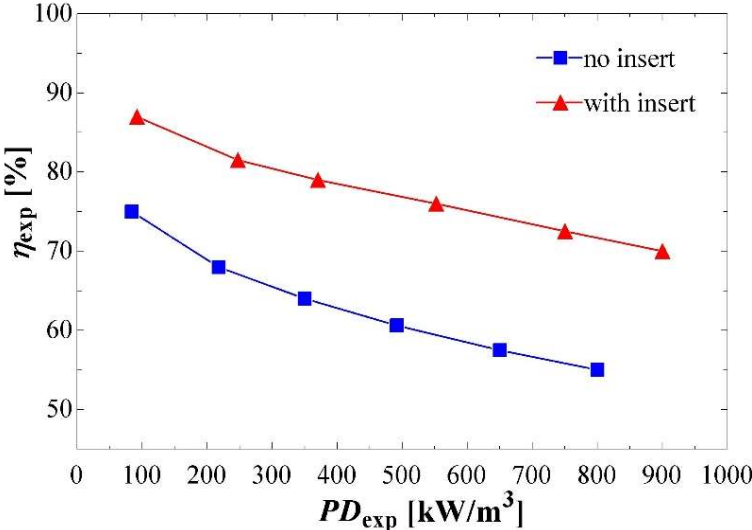
(b)

Figure 11. Efficiency against power density for the baseline case (no insert) and with parallel-

plate inserts case for: (a) compression process with an initial pressure of 8 bar, a final pressure of 200 bar, and power densities from 400 kW/m^3 to 800 kW/m^3 corresponding to compression durations from 2.8 s to 23 s and water flow rates from 420 L/min to 18 L/min, and (b) expansion process with an initial pressure of 200 bar, a final pressure of 2 bar, and power densities from 90 kW/m^3 to 900 kW/m^3 corresponding to expansion durations from 1 s to 8.5 s and water flow rates from 360 L/min to 55 L/min.

5.2.1 Thermodynamic performance analysis

In this section, a detailed energy analysis of the whole CAES system is performed using the validated model for a realistic condition in which air is compressed to 200 bar in the LPGC/E. Different performance indicators for a single-stroke compression/expansion process in the LPGC are presented in Table 7 and Table 8. The presented parameters in these two tables are used in energy analysis of the CAES systems. According to Table 7 and Table 8 compression and expansion occur in around 6 s and 3 s, respectively. The input work is decreased in the case of LPGC with plates and the expansion work is improved in the case of LPGC with plates or preheating the air compared to the base case. Note that the expansion efficiency of the CAES$_{PCM}$, CAES$_{PCM\&plates}$ and CAES$_{heater}$ is lower than the base case because the expansion efficiency for these three configurations is calculated based on isothermal expansion of preheated air.

Table 7. Thermodynamic performance indicators for a single compression stroke of the LPGC in different CAES configurations.

Configuration	W_{in} (kJ)	$E_{s,comp}$ (kJ)	PD_{comp} (kW/m^3)	η_{comp} (%)	t_{comp} (s)
CAES$_{base}$	30.7	22.3	453	73	5.7
CAES$_{plates}$	25.5	21.3	448	84	5.5
CAES$_{PCM}$	30.7	22.3	453	73	5.7
CAES$_{PCM\&plates}$	25.5	21.3	448	84	5.5
CAES$_{heater}$	30.7	22.3	453	73	5.7

Table 8. Thermodynamic performance indicators for a single expansion stroke of the LPGC in different CAES configurations.

Configuration	W_{out} (kJ)	$E_{s,exp}$ (kJ)	PD_{exp} (kW/m³)	η_{exp} (%)	t_{exp} (s)
CAES$_{base}$	5.7	8.1	228	71	2.9
CAES$_{plates}$	6.5	8.0	259	81	2.9
CAES$_{PCM}$	7.4	12.3	295	61	2.9
CAES$_{PCM\&plates}$	7.5	11.0	299	68	2.9
CAES$_{heater}$	7.4	12.3	295	61	2.9

In the following paragraph, the five configurations are compared in terms of the compressor power consumption, system power output during discharge, charging/discharging time, roundtrip and charging efficiencies. The thermodynamic properties (temperature, pressure, enthalpy) for different states of each configuration are shown in Table A1 in the Appendix. The results of this analysis are shown in Table 9.

The power consumption of the 9-bar compressor is 14.5 kWh for all five configurations. The charging and discharging time for all five configurations is around 3.5 h and 7 h, respectively. As discussed in the previous section, by insertion of the parallel plates in the LPGC/E, the compressor achieves a near-isothermal process. Hence, compared to the base-case configuration CAES$_{base}$, the CAES$_{plate}$ and CAES$_{PCM\&plates}$ systems require less compression work and pumping power to compress air. In the CAES$_{plate}$ and CAES$_{PCM\&plates}$, the amount of compressed air is around 4% less than CAES$_{base}$. According to Table 9, the power output of the base-case configuration CAES$_{base}$ is 14 kWh, which rises to 15.5 kWh with the introduction of parallel-plate inserts inside the LPGC/E. By heating the air using PCM heat exchanger or using a heater, increases the power output by 32% from 15.5 kWh for the base-case configuration CAES$_{base}$ to 18 kWh for the CAES$_{PCM}$ and CAES$_{heater}$ configurations. Combination of air heating and insertion the parallel plates, improves the power output from 15.5 kWh for the base-case configuration CAES$_{base}$ to 19.5 kWh for the CAES$_{PCM\&plates}$ configuration.

Compared to the base-case configuration, the roundtrip and charging efficiencies are significantly improved when heating the air before expansion using a PCM or a combination of PCM and parallel plates. For instance, the inclusion of parallel plates inside the LPGC/E (in the CAES$_{plates}$ configuration) improves the roundtrip efficiency from 40% for the base-case to 50% for

the CAES$_{plates}$ configuration. Additionally, the roundtrip efficiency increases from 40% for the CAES$_{base}$ to 52% and 63% for the CAES$_{PCM}$ and CAES$_{PCM\&plates}$ configurations, respectively.

Table 9. Thermodynamic performance indicators for the four CAES configurations in Figure 1.

	CAES$_{base}$	CAES$_{plates}$	CAES$_{PCM}$	CAES$_{PCM\&plates}$	CAES$_{heater}$	Unit
9-bar compressor power consumption	14.7	14.5	14.7	14.5	14.7	kWh
LPGC/E compression work	18.8	16.0	18.8	16.0	18.8	kWh
Pump work	19.6	16.8	19.6	16.8	19.6	kWh
Power output during discharge (LPGC/E expansion work)	14.2	16.0	18.5	20.5	18.5	kWh
Generated power	13.6	15.5	18.0	19.5	18.0	kWh
Discharge time	7.0	7.0	7.0	7.0	7.0	h
Charge time	3.5	3.5	3.5	3.5	3.5	h
200-bar air-storage tank volume	2.0	1.6	1.5	1.3	2.0	m^3
Roundtrip efficiency	40	50	52	63	42	%
Charge efficiency	43	53	56	66	45	%

In conclusion, the energy analysis provided here shows that inclusion of the parallel-plate inserts inside the LPGC/E improves the compression/expansion efficiencies of the LPGC/E and the whole CAES system. However, improvement on the CAES efficiency is not as significant as the configuration when the air is heated before expansion in the LPGC/E.

5.2.2 Technoeconomic results

A technoeconomic analysis is performed to investigate the cost benefit of using the proposed CAES system. Table 10 shows the effect of SEG on the payback period of these systems. In this section, we have investigated the payback period, total annual cost and annual profit of the system by considering a SEG of 5.5 p/kWh (6.8 ¢/kWh). Results show that the CAES$_{PCM\&plate}$ configuration has a significant effect on decreasing of the payback-period, CO_2 emission and fuel consumption compared to other configurations. The total investment cost of the CAES$_{PCM}$ is $15.8k, which is higher than the other configurations because of the extra purchase cost of the heat exchanger. Note that the total investment cost of the CAES$_{PCM\&plate}$ is lower than the CAES$_{PCM}$ as it needs a smaller size of the heat exchanger. Due to the high-power output of the CAES$_{PCM\&plate}$ configuration, the annual total income for this configuration is $2620, which is

higher than the other configurations. By comparing the dynamic payback period, it is seen that the CAES$_{PCM\&plate}$ and has the shortest payback period of 7 years. Although the annual total income for CAES$_{heater}$ is the same as the CAES$_{PCM}$, its roundtrip efficiency is lower than the CAES$_{PCM}$ configuration (see Table 7). This is because the CAES$_{heater}$ configuration, consumes a considerable amount of fuel to heat the compressed air before expanding in the LPGC/E. Using parallel plates inside the LPGC/E to achieve a near isothermal compression/expansion reduces the system's payback period by 5 years with respect to the base-case configuration.

Table 10 further shows the environmental impact of the five configurations analysed in the present work. Over the 20-yearsassumed lifetime of the proposed CAES systems, CO_2 emissions reduce by 36, 40, 46, 51 and 36 tonnes, respectively for the CAES$_{base}$, CAES$_{plate}$, CAES$_{PCM}$, CAES$_{PCM\&plate}$ and CAES$_{heater}$ configuration. Additionally, the proposed CAES systems help to save the fuel consumption by about 50 tonnes in CAES$_{base}$, 56 tonnes in CAES$_{plates}$, 65 tonnes in CAES$_{PCM}$, 71 tonnes in CAES$_{PCM\&plate}$ and 51 tonnes in CAES$_{heater}$ configuration. This fuel saving is the amount of natural gas required to produce the same amount of power output in a conventional power system.

Table 10. Comparison of the technoeconomic performance of the four CAES system configurations considering a 5.5 p/kWh (6.8 ¢/kWh) SEG and an economic lifetime of 20 years.

	CAES$_{base}$	CAES$_{plates}$	CAES$_{PCM}$	CAES$_{PCM\&plates}$	CAES$_{heater}$	Unit
Total investment cost	14.0	13.5	15.8	14.0	14.3	k\$
Annual total cost	940	790	840	690	840	\$
Annual total income	1840	2080	2380	2620	2380	\$
Annual total profit	900	1290	1540	1930	1540	\$
Dynamic payback period	15.5	10.5	10.0	7.0	9.0	Year
Fuel saving (natural gas)	50	56	65	71	51	Tonne
CO_2 emissions reduction	36	40	46	51	36	Tonne

Figure 12 compares the dynamic payback period (DPP) of the five systems with incentives and considering an SEG of 5.5 p/kWh (6.8 ¢/kWh) in 2020. With this SEG, all proposed CAES systems experience a payback period lower than 20 years lifetime of the systems. The CAES$_{PCM\&plate}$ and CAES$_{heater}$ has the shortest payback period of 7 years. In addition to this, all proposed systems except CAES$_{base}$ are found to be cost-effective even without renewable electricity incentive with a dynamic payback period of 15 years, 13 years, 10 years and 13 years for CAES$_{plate}$, CAES$_{PCM}$, CAES$_{PCM\&plate}$ and CAES$_{heater}$, respectively.
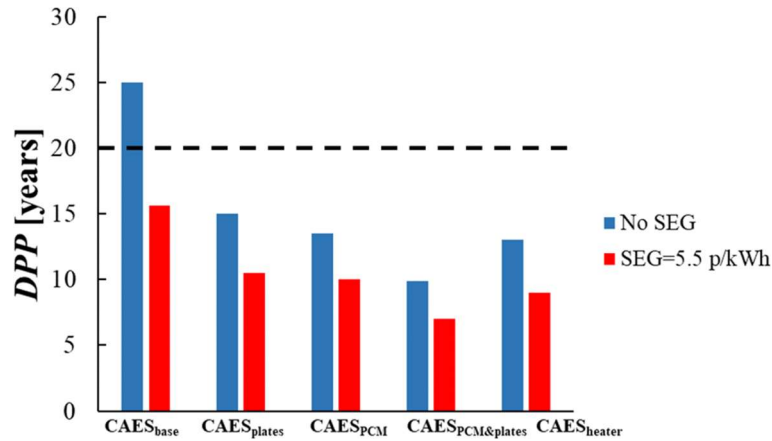
Figure 12. Effect of 5.5 p/kWh (6.8 ¢/kWh) SEG in 2020 on the dynamic payback period (*DPP*) of CAES_base, CAES_plate, CAES_PCM, CAES_PCM&plate and CAES_heater configurations.

6.   Further discussion and comparisons

A novel small-scale (20 kWh) overground compressed-air energy storage system was analysed in this work and found to have a roundtrip efficiency of 63%, which is promising given that it is higher than the efficiencies of existing conventional large-scale underground CAES systems, namely the Huntorf plant in Germany (290 MWe) and the McIntosh plant in the USA (110 MWe), which have efficiencies of 43% and 54%, respectively. Currently, there are no commercially available adiabatic CAES (A-CAES) products on the market, although there are numerous pilot-scale A-CAES projects under development, reflecting the promising role that A-CAES technology can play in future energy systems. Of note is the fact that the A-CAES pilot-scale systems under development currently have relatively low efficiencies around 20%, e.g., 23% is reported in Ref. [20]. Compared to large-scale CAES systems that are generally proposed for locations close to power generation sites, small-scale CAES systems would not have geological or other geographical limitations, and could be installed close to the point of electricity use, thereby providing better coupling between energy supply, storage and demand, which is a major requirement for the development of future decentralised micro-grid networks.

For electricity storage at very small scales (< 10 kWh), it is well-accepted that batteries are the most mature technology, which is commercially ready and proven for various applications. Therefore, a significant fraction of current research has been dedicated to reducing the costs and improving the lifetime of batteries for deployment at larger scales, particularly lithium-ion batteries that have a high roundtrip efficiencies, energy densities and peak power capabilities. Although the cost of lithium-ion batteries is falling rapidly, their cost per unit

power density is still high compared to thermomechanical storage systems, while low cycling times and lifetimes (~5-10 years), high degradation and captaincy reduction (~60-70%), high maintenance costs, toxicity and safety are considered barriers for such deployment, and further, batteries are less suitable for long-duration storage (days, weeks, etc.) and any application where the energy inputs and local demands can be diverse enough to include heating and/or cooling.

One available battery storage product with a small-scale capacity of 20 kWh (similar to the storage system developed here), which can be integrated with solar photovoltaic (PV) systems, is the Powervault 3, a lithium-polymer (Li-MNC) battery manufactured by Powervault [67-69]. This product has a stated lifetime of 10 years and an investment cost of ~$18,700 (£15,170) including VAT [69], leading to payback periods that are longer than its lifetime. It must be noted here that these battery systems have high roundtrip efficiencies of >90%, although, it is known that this can drop down below 70% over their lifetime. By contrast, the CAES system proposed here (configuration $CAES_{PCM\&plates}$ as per Table 10) has a payback period of 7 years, a lifetime of (at least) 20 years and a total investment cost that is projected, under favourable conditions, to be as low ~2.6 times lower than the aforementioned battery option for the same capacity system. Such CAES systems, like all thermomechanical storage systems, are non-toxic and can maintain performance over long periods with little degradation over their lifetime. Additionally, such systems are highly suitable for long-duration storage and flexible enough to be deployed in applications where surplus heat and/or cooling is available locally and required by the end user.

7. Conclusions

In this work, a small-scale (20 kWh) overground compressed-air energy storage (CAES) system using a novel reversible and near-isothermal liquid-piston gas compressor/expander (LPGC/E) was developed and tested for the first time. Comprehensive experimental, thermodynamic, technoeconomic and environmental assessments were conducted to analyse the performance of this proposed system. A testing facility was developed and experiments were conducted to collect data for validation of a mass-lumped model, specifically developed for this system.

Based on this model, a detailed study of the system was then performed in order to investigate and compare the efficiencies, costs, payback times and CO_2 emission reductions of five possible CAES system configurations featuring a LPGC/E, namely: (1) $CAES_{base}$, which is the base-case configuration; (2) $CAES_{plate}$, in which parallel plates are inserted into the LPGC/E as a heat exchanger for achieving near-isothermal compression and expansion; (3) $CAES_{PCM}$, in which a phase change material (PCM) is employed to store thermal energy from the compressed

air during the charge process that is later recovered for use during discharge; (4) $CAES_{PCM\&plate}$, which is a combination of the $CAES_{plate}$ and $CAES_{PCM}$ arrangements; and (5) $CAES_{heater}$, in which a heater is utilised instead of the PCM to preheat the compressed air during discharge. The main conclusions from this work are summarised below:

1. Compared to the base-case configuration, the $CAES_{PCM}$ and $CAES_{PCM\&plate}$ configurations show significantly improved roundtrip and charging electricity efficiencies. Relative to the base-case, the $CAES_{PCM\&plate}$ system has the highest roundtrip efficiency of 63%.

2. All proposed CAES system configurations, except the $CAES_{base}$ base case, can be cost-effective even without incentives. When considering a SEG intensive (5.5 p/kWh or 6.8 ¢/kWh) for renewable electricity generation, the dynamic payback period of the $CAES_{PCM\&plate}$ and $CAES_{heater}$ configurations have the shortest payback period of 7 years.

3. Over a 20-year lifetime, CO_2 emission reductions of 36, 40, 46, 51 and 36 tonnes can arise when employing the $CAES_{base}$, $CAES_{plate}$, $CAES_{PCM}$, $CAES_{PCM\&plate}$ and $CAES_{heater}$ configurations, respectively. The proposed CAES systems show a potential for reducing fuel consumption by about 50, 56, 65, 71 and 51 tonnes, respectively.

References

1. Aneke, M. and Wang, M., 2016. Energy storage technologies and real life applications–A state of the art review. *Applied Energy*, *179*, pp. 350-377.
2. Frate, G.F., Ferrari, L. and Desideri, U., 2020. Multi-criteria economic analysis of a pumped thermal electricity storage (PTES) with thermal integration. Front. *Energy Res*, *8*, p. 53.
3. Steinmann, W.D., 2014. The CHEST (Compressed Heat Energy STorage) concept for facility scale thermo mechanical energy storage. *Energy*, *69*, pp. 543-552.
4. Laughlin, R.B., 2017. Pumped thermal grid storage with heat exchange. *Journal of Renewable and Sustainable Energy*, *9*(4), p. 044103.

5. White, A., Parks, G. and Markides, C.N., 2013. Thermodynamic analysis of pumped thermal electricity storage. *Applied Thermal Engineering*, *53*(2), pp. 291-298.

6. Desrues, T., Ruer, J., Marty, P. and Fourmigue, J.F., 2010. A thermal energy storage process for large scale electric applications. *Applied Thermal Engineering*, *30*(5), pp. 425-432.

7. Thess, A., 2013. Thermodynamic efficiency of pumped heat electricity storage. *Physical Review Letters*, *111*(11), p. 110602.

8. Antonelli, M., Barsali, S., Desideri, U., Giglioli, R., Paganucci, F. and Pasini, G., 2017. Liquid air energy storage: Potential and challenges of hybrid power plants. *Applied Energy*, *194*, pp. 522-529.

9. Morgan, R., Nelmes, S., Gibson, E. and Brett, G., 2015. Liquid air energy storage–analysis and first results from a pilot scale demonstration plant. *Applied energy*, *137*, pp. 845-853.

10. Sciacovelli, A., Vecchi, A. and Ding, Y., 2017. Liquid air energy storage (LAES) with packed bed cold thermal storage–From component to system level performance through dynamic modelling. *Applied Energy*, *190*, pp. 84-98.

11. Guizzi, G.L., Manno, M., Tolomei, L.M. and Vitali, R.M., 2015. Thermodynamic analysis of a liquid air energy storage system. *Energy*, *93*, pp. 1639-1647.

12. Suberu, M.Y., Mustafa, M.W. and Bashir, N., 2014. Energy storage systems for renewable energy power sector integration and mitigation of intermittency. *Renewable and Sustainable Energy Reviews*, *35*, pp. 499-514.

13. Mahlia, T.M.I., Saktisahdan, T.J., Jannifar, A., Hasan, M.H. and Matseelar, H.S.C., 2014. A review of available methods and development on energy storage; technology update. *Renewable and Sustainable Energy Reviews*, *33*, pp. 532-545.

14. Akhil, A.A., Huff, G., Currier, A.B., Kaun, B.C., Rastler, D.M., Chen, S.B., Cotter, A.L., Bradshaw, D.T. and Gauntlett, W.D., 2013. DOE/EPRI 2013 electricity storage handbook in collaboration with NRECA (p. 163), Albuquerque, NM: Sandia National Laboratories.

15. Chen, H., Cong, T.N., Yang, W., Tan, C., Li, Y. and Ding, Y., 2009. Progress in electrical energy storage system: A critical review. *Progress in Natural Science*, *19*(3), pp. 291-312.

16. Ribeiro, P.F., Johnson, B.K., Crow, M.L., Arsoy, A. and Liu, Y., 2001. Energy storage systems for advanced power applications, *IEEE*, *89*, pp.1744-1756

17. Heidari M, Lemofouet S, Rufer A., 2014. On the strategies towards isothermal gas compression and expansion. 22nd International Compressor Engineering Conference, Purdue.

18. Zhou, Q., Du, D., Lu, C., He, Q. and Liu, W., 2019. A review of thermal energy storage in compressed air energy storage system. *Energy*, *188*, p. 115993.

19. Geissbühler, L., Becattini, V., Zanganeh, G., Zavattoni, S., Barbato, M., Haselbacher, A. and Steinfeld, A., 2018. Pilot-scale demonstration of advanced adiabatic compressed air energy storage, Part 1: Plant description and tests with sensible thermal-energy storage. *Journal of Energy Storage*, *17*, pp. 129-139.

20. Wang, S., Zhang, X., Yang, L., Zhou, Y. and Wang, J., 2016. Experimental study of compressed air energy storage system with thermal energy storage. *Energy*, *103*, pp. 182-191.

21. Van de Ven, J.D. and Li, P.Y., 2009. Liquid piston gas compression. *Applied Energy*, *86*(10), pp. 2183-2191.

22. Yan, B., Wieberdink, J., Shirazi, F., Li, P.Y., Simon, T.W. and Van de Ven, J.D., 2015. Experimental study of heat transfer enhancement in a liquid piston compressor/expander using porous media inserts. *Applied Energy*, *154*, pp. 40-50.

23. Wieberdink, J., Li, P.Y., Simon, T.W. and Van de Ven, J.D., 2018. Effects of porous media insert on the efficiency and power density of a high pressure (210 bar) liquid piston air compressor/expander–An experimental study. *Applied Energy*, *212*, pp. 1025-1037.

24. Solanki, R., Mathie, R., Galindo, A. and Markides, C.N., 2013. Modelling of a two-phase thermofluidic oscillator for low-grade heat utilisation: Accounting for irreversible thermal losses. *Applied Energy*, *106*, pp. 337-354.

25. Markides, C.N., Osuolale, A., Solanki, R. and Stan, G.B.V., 2013. Nonlinear heat transfer processes in a two-phase thermofluidic oscillator. *Applied energy*, *104*, pp. 958-977.

26. Saadat, M., Li, P.Y. and Simon, T.W., Optimal trajectories for a liquid piston compressor/expander in a Compressed Air Energy Storage system with consideration of heat transfer and friction, *2012 American Control Conference (ACC)*, Montreal, QC, Canada, pp. 1800-1805.

27. Zhang, C., Yan, B., Wieberdink, J., Li, P.Y., Van de Ven, J.D., Loth, E. and Simon, T.W., 2014. Thermal analysis of a compressor for application to compressed air energy storage. *Applied Thermal Engineering*, *73*(2), pp. 1402-1411.

28. Zhang, C., Simon, T.W. and Li, P.Y., 2014. Optimization of the axial porosity distribution of porous inserts in a liquid-piston gas compressor using a one-dimensional formulation. In *ASME International Mechanical Engineering Congress and Exposition*, American Society of Mechanical Engineers.

29. Zhang, C., Wieberdink, J., Simon, T.W., Li, P.Y., Van de Ven, J. and Loth, E., 2014. Numerical analysis of heat exchangers used in a liquid piston compressor using a one-dimensional model with an embedded two-dimensional submodel. In *ASME International Mechanical Engineering Congress and Exposition*, American Society of Mechanical Engineers.

30. Patil, V.C., Liu, J. and Ro, P.I., 2020. Efficiency improvement of liquid piston compressor using metal wire mesh for near-isothermal compressed air energy storage application. *Journal of Energy Storage*, *28*, p. 101226.

31. Patil, V.C. and Ro, P.I., 2020. Experimental study of heat transfer enhancement in liquid piston compressor using aqueous foam. *Applied Thermal Engineering*, *164*, p. 114441.

32. Wang, J., Ma, L., Lu, K., Miao, S., Wang, D. and Wang, J., 2017. Current research and development trend of compressed air energy storage. *Systems Science & Control Engineering*, *5*(1), pp. 434-448.

33. Luo, X., Wang, J., Dooner, M. and Clarke, J., 2015. Overview of current development in electrical energy storage technologies and the application potential in power system operation. *Applied Energy*, *137*, pp. 511-536.

34. Agarwal, T., 2012. Review of pump as turbine (PAT) for micro-hydropower. *International Journal of Emerging Technology and Advanced Engineering*, *2*(11), pp.163-169.

35. Kermani, N.A. and Rokni, M., 2015. Heat transfer analysis of liquid piston compressor for hydrogen applications. *International journal of Hydrogen Energy*, *40*(35), pp. 11522-11529.

36. Bejan, A., Tsatsaronis, G. and Moran, M.J., 1995. *Thermal Design and Optimization*. 4th ed. New York (NY). John Wiley & Sons.

37. Kreith, F., Manglik, R.M. and Bohn, M.S., 2012. *Principles of Heat Transfer*, SI eddition. 7th ed. Cengage Learning.

38. Cengel, Y.A. and Pérez, H., 2002. Heat Transfer: A Practical Approach. 2nd ed. McGraw-Hill Education.

39. Piya, C., Sircar, I., Van de Ven, J.D. and Olinger, D.J., 2009, January. Numerical modeling of liquid piston gas compression. In *ASME International Mechanical Engineering Congress and Exposition.* Florida, USA.

40. Khaljani M, Mahmoudi Y, Murphy A, Harrison J, Surplus D., 2019. Thermodynamic and heat transfer analysis of a Liquid Piston Gas Compressor (LPGC). *In 2019 International Conference on Innovative Applied Energy (IAPE'2019)*. Oxford, UK.

41. Khaljani, M., Saray, R.K. and Bahlouli, K., 2015. Comprehensive analysis of energy, exergy and exergo-economic of cogeneration of heat and power in a combined gas turbine and organic Rankine cycle. *Energy Conversion and Management*, *97*, pp. 154-165.

42. Safaei, H. and Aziz, M.J., 2017. Thermodynamic analysis of three compressed air energy storage systems: Conventional, adiabatic, and hydrogen-fueled. *Energies*, *10*(7), p. 1020.

43. Diyoke, C., Aneke, M., Wang, M. and Wu, C., 2018. Techno-economic analysis of wind power integrated with both compressed air energy storage (CAES) and biomass gasification energy storage (BGES) for power generation. *RSC advances*, *8*(39), pp. 22004-22022.

44. Saadat, M. and Li, P.Y., 2012, June. Modeling and control of a novel compressed air energy storage system for offshore wind turbine. In *2012 American Control Conference (ACC)* (pp. 3032-3037). IEEE.

45. Patil, V.C. and Ro, P.I., 2020. Modeling of liquid-piston based design for isothermal ocean compressed air energy storage system. *Journal of Energy Storage*, *31*, p. 101449.

46. Wang, P., Zhao, P., Xu, W., Wang, J. and Dai, Y., 2019. Performance analysis of a combined heat and compressed air energy storage system with packed bed unit and electrical heater. *Applied Thermal Engineering*, *162*, p. 114321.

47. Hu, W., Song, M., Jiang, Y., Yao, Y. and Gao, Y., 2019. A modeling study on the heat storage and release characteristics of a phase change material based double-spiral coiled heat exchanger in an air source heat pump for defrosting. *Applied Energy*, *236*, pp. 877-892.

48. Royo, P., Ferreira, V.J., Ure, Z., Gledhill, S., López-Sabirón, A.M. and Ferreira, G., 2020. Multiple-Criteria Decision Analysis and characterisation of phase change materials for waste heat recovery at high temperature for sustainable energy-intensive industry. *Materials & Design*, *186*, p. 108215.

49. El-Dessouky, H. and Al-Juwayhel, F., 1997. Effectiveness of a thermal energy storage system using phase-change materials. *Energy Conversion and Management*, *38*(6), pp. 601-617.

50. PCM Products, PCM, April 2020. [Online]. Available: http://www.pcmproducts.net/phase_change_material_products.html. [Accessed 20 March 2020].

51. Pierobon, L., Nguyen, T.V., Larsen, U., Haglind, F. and Elmegaard, B., 2013. Multi objective optimization of organic Rankine cycles for waste heat recovery: Application in an offshore platform. *Energy*, *58*, pp. 538-549.

52. Towler, G. and Sinnott, R., 2012. *Chemical Engineering Design: Principles, Practice and Economics of Plant and Process Design*. 2nd ed. Elsevier.

53. Yanadori, M. and Masuda, T., 1989. Heat transfer study on a heat storage container with a phase change material. (Part 2. Heat transfer in the melting process in a cylindrical heat storage container). *Solar Energy*, *42*(1), pp. 27-34.

54. Ofgem, Tariffs and payments: Domestic RHI, Ofgem, 31 March 2020. [Online]. Available: https://www.ofgem.gov.uk/environmental-programmes/domestic-rhi/contacts-guidance-and-resources/tariffs-and-payments-domestic-rhi/current-future-tariffs. [Accessed 22 April 2020].

55. Ramadan, O., Omer, S., Ding, Y., Jarimi, H., Chen, X. and Riffat, S., 2018. Economic evaluation

of installation of standalone wind farm and wind+ CAES system for the new regulating tariffs for renewables in Egypt. *Thermal Science and Engineering Progress*, *7*, pp. 311-325.

56. Luo, X., Wang, J., Dooner, M., Clarke, J. and Krupke, C., 2014. Overview of current development in compressed air energy storage technology. *Energy Procedia*, *62*, pp. 603-611.

57. Hennecke, F., A comparative study of pump life cycle costs.WannerHydra-Cell, 2006. [Online]. Available: https://www.hydra-cell.co.uk/docs/PT20-27.pdf. [Accessed 6 July 2020].

58. Couper, J.R., Penney, W.R. and Fair, J.R., 2009. *Chemical Process Equipment-Selection and Design.* 2nd Edition. Gulf Professional Publishing.

59. Zhang, X., Zeng, R., Deng, Q., Gu, X., Liu, H., He, Y., Mu, K., Liu, X., Tian, H. and Li, H., 2019. Energy, exergy and economic analysis of biomass and geothermal energy based CCHP system integrated with compressed air energy storage (CAES). *Energy Conversion and Management*, *199*, p. 111953.

60. Sayyaadi, H. and Nejatolahi, M., 2011. Multi-objective optimization of a cooling tower assisted vapor compression refrigeration system. *International Journal of Refrigeration*, *34*(1), pp. 243-256.

61. Bulb, Smart tariff electricity rates during British Summer Time,Bulb, 2020. [Online]. Available: https://bulb.co.uk/smart. [Accessed 30 March 2020].

62. Global Petrol Prices, LPG prices, United Kingdom LPG prices, Global Petrol Prices, 2020. [Online]. Available: https://www.globalpetrolprices.com/United-Kingdom/lpg_prices. [Accessed 30 March 2020].

63. Herrando, M., Ramos, A. and Zabalza, I., 2018. Cost competitiveness of a novel PVT-based solar combined heating and power system: Influence of economic parameters and financial incentives. *Energy Conversion and Management*, *166*, pp. 758-770.

64. Office for National Statistics, Consumer price inflation, Office for National Statistics, 2020. [Online]. Available: https://www.ons.gov.uk/economy/inflationandpriceindices/bulletins/consumerpriceinflation/may2020. [Accessed 7 July 2020]

65. Department for Business, Energy and Industrial Strategy, 2019 Government Greenhouse Gas Conversion Factors for Company Reporting, 2019. [Online]. Available: https://assets.publishing.service.gov.uk/government/uploads system/uploads/attachment_data/file/829336/2019_Green-house-gas-reporting-methodology.pdf. [Accessed 2 July 2020].

66. Herrando, M. and Markides, C.N., 2016. Hybrid PV and solar-thermal systems for domestic heat and power provision in the UK: Techno-economic considerations. *Applied Energy*, *161*, pp. 512-532.

67. POWERVAULT, Technical, Technical specification, 2020. [Online]. Available: https://www.powervault.co.uk/technical/technical-specifications [Accessed 7 December 2020].

68. Solar guide, Solar Battery, 2020. [Online]. Available: https://www.solarguide.co.uk/solar-batteries/powervault-g200# [Accessed 7 December 2020].

69. ELECTRICCARHOME, Battery Storage, 2020. [Online]. Available: https://electriccarhome.co.uk/battery-storage/powervault [Accessed 7 December 2020].

70. Mathie, R., Markides, C.N. and White, A.J., 2014. A framework for the analysis of thermal losses in reciprocating compressors and expanders. Heat Transfer Engineering, *35*, pp. 1435-1449.

Appendix

Table A1 shows the conditions of the air and water phases at all key thermodynamic states in the five studied CAES configurations. The states are all defined in Figure 1. The CAES$_{heater}$ conditions are the same as those for CAES$_{PCM}$, except for State 18, at which the fuel enters the heater at ambient conditions in the CAES$_{heater}$ configuration.

Table A1. Thermodynamic properties of the four CAES systems at each state in Figure 1.

State	Fluid	CAES$_{base}$				CAES$_{plates}$				CAES$_{PCM}$/CAES$_{heater}$				CAES$_{PCM\&plates}$			
		T	P	h	$\dot{m}$	T	P	h	$\dot{m}$	T	P	h	$\dot{m}$	T	P	h	$\dot{m}$
1	Air	298	1.0	299	0.0142	298	1.0	299	0.0141	298	1.0	299	0.0142	298	1.0	299	0.0141
2	Air	582	9.0	596	0.0142	582	9.0	596	0.0141	582	9.0	596	0.0142	582	9.0	596	0.0141
3	Air	298	9.0	299	0.0142	298	9.0	299	0.0141	298	9.0	299	0.0142	298	9.0	299	0.0141
4	Air	298	9.0	299	0.0142	298	9.0	299	0.0141	298	9.0	299	0.0142	298	9.0	299	0.0141
5	Air	298	8.0	299	0.0142	298	8.0	299	0.0141	298	8.0	299	0.0142	298	8.0	299	0.0141
6	Air	579	200	585	0.0142	470	200	471	0.0141	579	200	585	0.0142	470	200	471	0.0141
7	Air	579	200	585	0.0142	470	200	471	0.0141	579	200	585	0.0142	470	200	471	0.0141
8	Water	298	1.0	105	1.40	298	1.0	105	1.40	298	1.0	105	1.40	298	1.0	105	1.40
9	Water	301	200	128	1.40	3001	200	129	1.40	301	200	128	1.40	3001	200	129	1.40
10	Water	299	200	128	1.40	299	200	129	1.40	299	200	128	1.40	299	200	129	1.40
11	Water	301	200	137	1.40	301	200	137	1.40	301	200	137	1.40	301	200	137	1.40
12	Water	305	1.0	137	1.40	305	1.0	137	1.40	305	1.0	137	1.40	305	1.0	137	1.40
13	Air	298	200	263	0.006	298	200	263	0.007	298	200	263	0.006	298	200	263	0.006
14	Air	298	2.0	298	0.006	297	2.0	298	0.007	298	2.0	298	0.006	298	2.0	298	0.006
15	Water	298	200	123	2.80	298	200	123	2.80	298	200	123	2.80	298	200	123	2.80
16	Water	298	200	123	2.80	298	200	123	2.80	298	200	123	2.80	298	200	123	2.80
17	Water	298	2.0	106	2.80	298	2.0	106	2.80	298	2.0	106	2.80	298	2.0	106	2.80
18	-	-	-	-	-	-	-	-	-	436	200	437	0.006	383	200	384	0.006
19	-	-	-	-	-	-	-	-	-	430	200	431	0.006	376	200	377	0.006

The units of the parameters are: T [K], P [bar], h [kJ Kg^{-1}] and $\dot{m}$ [kg s^{-1}].

44